

Article

https://doi.org/10.1038/s41467-025-64484-x

A red fluorescent genetically encoded biosensor for in vivo imaging of extracellular L-lactate dynamics

Received: 26 February 2025

Accepted: 18 September 2025

Published online: xx xx 2025



Yuki Kamijo¹, Philipp Mächler^{2,16}, Natalie Ness © ^{3,4,16}, Cong Quang Vu © ^{5,16}, Tsukasa Kusakizako © ^{6,16}, Jamsad Mannuthodikayil⁷, Zaneta Ku², Marc Boisvert⁸, Ekaterina Grebenik⁹, Ikumi Miyazaki © ¹, Rina Hashizume¹, Haruaki Sato © ¹⁰, Rui Liu © ², Yukiko Hori © ¹⁰, Taisuke Tomita © ¹⁰, Tetsuro Katayama¹¹, Akihiro Furube © ¹¹, Gabriela Caraveo ⁹, Marie-Eve Paquet © ^{8,12}, Mikhail Drobizhev © ¹³, Osamu Nureki ⁶, Satoshi Arai © ⁵, Marco Brancaccio © ^{3,4}, Robert E. Campbell © ^{1,8,12}, David Kleinfeld © ^{2,14} & Yusuke Nasu © ^{1,7,15}

L-Lactate is increasingly recognized as an intercellular energy currency in mammals, but mysteries remain regarding the spatial and temporal dynamics of its release and uptake between cells via the extracellular environment. Here we introduce R-eLACCO2.1, a red fluorescent extracellular L-lactate biosensor that is superior to previously reported green fluorescent biosensors in in vivo sensitivity to increases in extracellular L-lactate and spectral orthogonality. R-eLACCO2.1 exhibits excellent fluorescence response in cultured cells, mouse brain slices, and live mice, R-eLACCO2.1 also serves as an effective fluorescence lifetime-based biosensor. Using R-eLACCO2.1, we monitor whisker stimulation and locomotion-induced changes in endogenous extracellular L-lactate in the somatosensory cortex of awake mice. To highlight the potential insights gained from in vivo measurements with R-eLACCO2.1, we perform dual-color imaging from the somatosensory cortex of actively locomoting mice. This enables us to simultaneously observe the neural activity, reported by a green fluorescent GCaMP calcium ion biosensor, and extracellular L-lactate. As the high-performance tool in the suite of extracellular L-lactate biosensors, R-eLACCO2.1 is ideally suited to delimit the emerging roles of L-lactate in mammalian metabolism.

Living cells catabolize glucose into L-lactate for biologically-useful energy. This process has been historically linked to muscle fatigue and viewed negatively due to its association with acidosis in conditions such as sepsis and hypoxia¹⁻³. However, recent studies have contradicted this view by demonstrating L-lactate's vital role as an intercellular and interorgan exchangeable fuel source in a range of tissues⁴. As one example, the astrocyte-to-neuron lactate shuttle (ANLS) hypothesis proposes that astrocytes preferentially metabolize glucose and glycogen to L-lactate, which is then released to the extracellular

environment and taken up by neurons^{5,6}. Once in neurons, the L-lactate is used for the production of adenosine triphosphate (ATP) to provide the energy necessary to sustain heightened neural activity^{5,7}. In addition to the role of L-lactate as an energetic substrate, there has been a growing appreciation of its role as a signaling molecule in a variety of tissues of mammals. In neurons, imported L-lactate perturbs the intracellular redox state, hence stimulating the expression of genes related to neuronal plasticity, long-term memory, and social behavior^{5,7,8}. Disruption of L-lactate signaling is associated with diverse

A full list of affiliations appears at the end of the paper. e-mail: nasu@as.edu.tw



pathological conditions such as Alzheimer's disease, amyotrophic lateral sclerosis, depression, and schizophrenia^{9,10}.

To address fundamental questions on such cell-to-cell L-lactate. including the ANLS hypothesis that remains controversial with evidence both for^{5,6} and against it¹¹, improved methods for monitoring extracellular L-lactate are necessary. Enzyme-based electrodes, though useful for in vivo measurements, suffer from limited spatial resolution and invasive tissue disruption¹². A promising alternative would be a genetically encoded fluorescent biosensor based on the combination of a fluorescent protein and an L-lactate binding protein¹³. Introduction of the gene encoding such a biosensor into an organism would enable the expression of the biosensor in tissues of interest, enabling in vivo fluorescence imaging of extracellular L-lactate dynamics with high spatiotemporal resolution. Researchers have reported genetically encoded fluorescent biosensors for imaging intracellular L-lactate using fluorescence intensity¹⁴⁻²¹ or fluorescence lifetime²². In an effort to realize an ideal genetically encoded fluorescent biosensor for extracellular L-lactate, we have previously developed eLACCO1.1 (Ref. 23) and its improved version eLACCO2.1 (Ref. 20). These biosensors have facilitated minimally invasive imaging of extracellular L-lactate in cultured cells and living mice, opening the door to a range of potential biological applications in which the dynamics of extracellular L-lactate are investigated in vivo. Despite their utility and advantages, both versions exhibit green fluorescence that constrains their utility for multiplexed imaging applications, such as the concurrent monitoring of L-lactate and neuronal activity (e.g., with a GCaMP calcium ion (Ca²⁺) biosensor²⁴).

Here, we report the development of a genetically encoded red fluorescent biosensor for extracellular L-lactate. This biosensor, designated R-eLACCO2.1, is highly optimized for cell surface expression and exhibits a large fluorescence intensity change in response to extracellular L-lactate in live mammalian cells, mouse brain slices, and live mice. Serendipitously, we find that R-eLACCO2.1 also serves as an effective biosensor for fluorescence lifetime imaging microscopy (FLIM). We demonstrate that R-eLACCO2.1 enables multiplex imaging of extracellular L-lactate and neural activities in combination with a green fluorescent Ca²⁺ biosensor in awake mice.

Results

Development of a genetically encoded red fluorescent L-lactate biosensor, R-eLACCO2

To construct an initial prototype red fluorescent L-lactate biosensor (Fig. 1a), we swapped the circularly permuted green fluorescent protein (cpGFP) of the green L-lactate biosensor eLACCO1 for the circularly permuted red fluorescent protein (cpmApple) (Supplementary Fig. 1a)²³. The resulting variant, designated R-eLACCO0.1, showed a slight increase in fluorescence intensity $(\Delta F/F = (F_{\text{max}} - F_{\text{min}})/F_{\text{min}} = 0.2)$ upon treatment with L-lactate (Supplementary Fig. 1b). To develop variants of R-eLACCO0.1 with larger $\Delta F/F$, we performed directed evolution with screening for L-lactate-dependent change in fluorescence intensity (Fig. 1b). This effort produced the R-eLACCO1 variant with $\Delta F/F$ of 4.3 (Fig. 1c and Supplementary Figs. 2 and 3a,b). To tune ReLACCOI's affinity, we introduced the conservative Leu79lle mutation to produce the low-affinity R-eLACCO1.1 variant with $\Delta F/F$ of 3.9 and apparent $K_d = 1.4 \text{ mM}$ (Supplementary Fig. 3c-j). To our disappointment, fluorescence imaging revealed that R-eLACCO1.1 expressed on the cell surface was only dimly fluorescent, and the fluorescence response to L-lactate was limited ($\Delta F/F \sim 1$) (Supplementary Fig. 3k).

To improve the expression level and $\Delta F/F$ in living cells, we further performed directed evolution using R-eLACCO1 as a starting template (Fig. 1b,c and Supplementary Fig. 2). One round of site-directed optimization, followed by eleven rounds of directed evolution by random mutagenesis of the whole gene, produced the high-performance variant R-eLACCO1.93 with $\Delta F/F$ of 18 (Fig. 1c). During this directed evolution process, we had identified a beneficial mutation (Ile191Val) in a

variant that was not part of the lineage that led to R-eLACCO1.93. Introduction of this Ile191Val mutation to R-eLACCO1.93 was the final step towards a highly optimized variant, designated R-eLACCO2 (Fig. 1d). R-eLACCO2 contains a total of 25 mutations relative to R-eLACCO0.1 (Supplementary Fig. 4). We undertook a comprehensive characterization of the biochemical and spectral attributes of R-eLACCO2, its low-affinity variant R-eLACCO2.1, and a non-responsive control variant R-deLACCO_{ctrl} (Fig. 1e–k, Table 1, Supplementary Fig. 5, Supplementary Table 1, and Supplementary Note 1), and found that R-eLACCO2 variants also function as a FLIM biosensor (Fig. 1l,m and Supplementary Fig. 6).

To obtain structural insight into the mechanism of ReLACCO2, we determined the cryo-EM structure of R-eLACCO2 in the L-lactate bound state at a global resolution of 2.7 Å (Fig. 1n, Supplementary Fig. 7, and Supplementary Note 2). The density map enabled the modeling of lactate-bound R-eLACCO2, using the crystal structure of eLACCO1 (PDB 7E9Y)²³ and cpmApplebased Ca2+ biosensor R-GECO1 (PDB 4I2Y)25 for TTHA0766 and cpmApple domain, respectively (Fig. 1n and Supplementary Table 2). In the lactate-bound state of R-eLACCO2, the tyrosinederived phenolate group of the chromophore forms an electrostatic interaction with the protonated amine group of Lys211 that is located on an adjacent β-strand of the cpmApple domain (Fig. 10). Note that these charge states (i.e., phenolate anion and protonated amine cation) are inferred as the cryo-EM structure that does not have sufficient resolution to enable the location of protons to be determined. Lys211Glu mutation led to an inverse fluorescence response (Supplementary Fig. 8), suggesting the critical role of Lys211 in modulating the fluorescence of R-eLACCO2.

Optimization of cell surface localization

Our previous work on eLACCO2.1 had demonstrated that the combination of N-terminal leader sequence and C-terminal anchor domain plays an essential role in the performance of the extracellular targeted biosensor²⁰. To identify the best leader-anchor combination for R-eLACCO2.1, we first examined the efficiency of cell surface targeting with a human CD59-derived leader sequence and a range of anchor domains (Fig. 2a,b). Colocalization analyses of R-eLACCO2.1 and a green fluorescent cell surface marker revealed that all protein-based anchors resulted in only intracellular expression. In contrast, all glycosylphosphatidylinositol (GPI)-based anchors resulted in efficient targeting to the cell surface. Three (CD59, COBRA, and GFRA1) of the four GPI-based anchors investigated resulted in a high proportion of biosensors localized on the cell surface.

We next screened various N-terminal leader sequences in combination with the CD59 GPI anchor (Fig. 2c). Of 14 leader sequences examined, two (SPARC and cholera toxin) resulted in only intracellular localization, while the other twelve gave excellent membrane localization of R-eLACCO2.1. This result suggests that both the C-terminal anchor and the N-terminal leader sequence can influence targeting to the cell surface. Three leader sequences (HA, Igk, and pat-3) provided the brightest fluorescent signals and were therefore chosen as the most promising leader sequences. To determine the best combination of the leader sequences and anchor domains, we combined the most promising leader sequences (HA, $\lg \kappa$, and pat-3) and anchor domains (CD59, COBRA, and GFRA1), and measured $\Delta F/F$ of each combination in HeLa cells upon treatment of 10 mM L-lactate (Fig. 2d). This measurement revealed that R-eLACCO2.1 with the Igκ-derived N-terminal leader sequence and the COBRA-based C-terminal anchor exhibited the highest fluorescence response to L-lactate. R-eLACCO2.1 with this best leader-anchor combination shows $\Delta F/F$ of ~5, which is approximately 5× higher than R-eLACCO1.1 with the CD59-derived leader and anchor combination (Supplementary Fig. 3k).

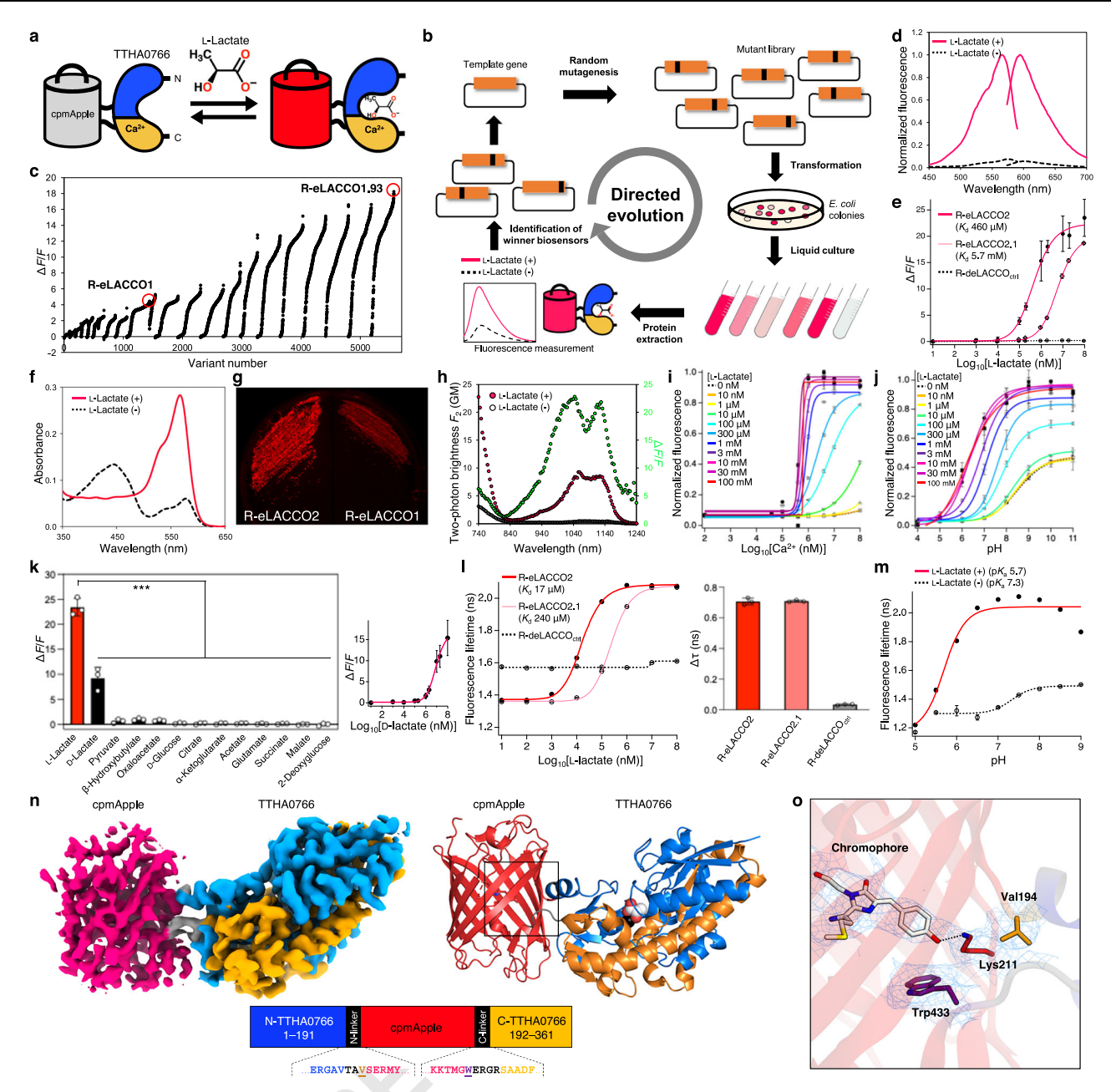


Fig. 1 | **Development and in vitro characterization of R-eLACCO2.** a Schematic representation of R-eLACCO and its mechanism of response to L-lactate. **b** Schematic of directed evolution workflow. **c** $\Delta F/F$ rank plot representing all proteins tested during the directed evolution. **d** Excitation and emission spectra of R-eLACCO2 in the presence (10 mM) and absence of L-lactate. **e** Dose-response curves of R-eLACCO2, R-eLACCO2.1, and R-deLACCO2, for L-lactate. n=3 experimental triplicates (mean ± s.d.). **f** Absorbance spectra of R-eLACCO2 in the presence (50 mM) and absence of L-lactate. **g** Fluorescence image of a streak plate of *E. coli* expressing R-eLACCO1 or R-eLACCO2. **h** Two-photon excitation spectra of R-eLACCO2 in the presence (10 mM) and absence of L-lactate. $\Delta F/F$ is represented in the green plots. GM, Goeppert-Mayer units. **i** Dose-response curve of R-eLACCO2 as a function of Ca²⁺ in various L-lactate concentrations. Fluorescence intensities were normalized based on the largest fluorescence value in the graph. n=3 experimental triplicates (mean ± s.d.). **j** pH titration curves of R-eLACCO2 in various L-lactate concentrations. Fluorescence intensities were normalized based on the

largest fluorescence value in the graph. n=3 experimental triplicates (mean \pm s.d.). **k** Specificity of R-eLACCO2. Concentration of each metabolite is 10 mM. Right graph represents a dose-response curve of R-eLACCO2 for D-lactate. n=3 experimental triplicates (mean \pm s.d.). One-way analysis of variance (ANOVA) with the Dunnett's post hoc tests. ***p<0.0001. ***p (Dunnett's, each metabolite vs. L-lactate as a control group) <0.0001. **l** Dose-lifetime curves (left) and $\Delta \tau$ (right) of R-eLACCO2, R-eLACCO2.1, and R-deLACCO $_{\rm ctrl}$ for L-lactate. n=3 experimental triplicates (mean \pm s.d.). **m** pH-lifetime curves of R-eLACCO2 in the presence (100 mM) and absence of L-lactate. n=3 experimental triplicates (mean \pm s.d.). **n** Cryo-EM structure of R-eLACCO2 in the lactate bound state. L-Lactate and Ca²⁺ (black) are shown in sphere representations. **o** Density map and constructed model of the chromophore. The two "gate post" residues (Val194 and Trp433)¹³ in cpmApple of R-eLACCO2 are highlighted in dark orange and purple, respectively. Source data are provided as a Source Data file.

Characterization of R-eLACCO2 variants in live mammalian cells We characterized R-eLACCO2 variants with the optimized leader (Igk) and anchor (COBRA) expressed in mammalian cells (Fig. 3a). The application of 10 mM L-lactate resulted in a robust increase in

fluorescence intensity of R-eLACCO2 ($\Delta F/F$ of 4.5 ± 0.1, mean ± s.e.m.) and R-eLACCO2.1 ($\Delta F/F$ of 6.2 ± 0.2, mean ± s.e.m.) expressed on the surface of HeLa cells (Fig. 3b,c). The control biosensor R-deLACCO_{ctrl} had similar membrane localization and, as expected, did not respond

Table 1 | One- and two-photon photophysical parameters

L-Lactate	R-eLACCO1.1		R-eLACCO2		R-iLACCO1 (Ref. 20)		R-GECO1 (Refs. 32,52)		mApple
	-	+	-	+	-	+	_a	+ ^a	- (Ref. 73)
One-photon parameters									
iFluorescence excitation max- imum (nm)	577	565	578	566	574	564	577	561	569
Fluorescence emission max- imum (nm)	599	593	602	594	604	594	600	589	591
Neutral absorbance peak (nm)	443	ND	444	ND	444	447	445	445	N/A
Anionic absorbance peak (nm)	576	563	578	567	579	561	577	561	N/A
Relative fraction of neutral chromophore, $\rho_{\rm N}$	0.75	0.55	0.88	0.35	0.95	0.39	0.94 ^b	0.18 ^b	0.17°
Relative fraction of anionic chromophore, $\rho_{\rm A}$	0.25	0.45	0.12	0.65	N/A	0.61	0.06 ^b	0.82 ^b	0.83°
Neutral extinction coefficient, ε_{N} (mM ⁻¹ cm ⁻¹)	35	ND	35	40	36	55	33	30	N/A
Anionic extinction coefficient, ϵ_A (mM ⁻¹ cm ⁻¹)	91	91	110	110	84	88	89	69	75
Neutral quantum yield, $\phi_{ m N}$	ND	ND	ND	ND	N/A	N/A	N/A	N/A	N/A
Anionic quantum yield, ϕ_{A}	0.16	0.24	0.11	0.28	0.17	0.21	0.15	0.21	0.46
Molecular brightness, $\rho_A \times \varepsilon_A \times \varphi_A$	3.6	9.8	1.5	20	N/A	11	0.80	12	29
Fluorescence lifetime (ns)	1.7 ^d	1.7 ^d	1.4 ^d 1.4 ^e	2.1 ^d 2.2 ^e	N/A	N/A	N/A	N/A	N/A
Radiative rate constant, $k_{\rm r}$ (10 ⁸ s ⁻¹)	0.97 ^d	1.4 ^d	0.8 ^d 0.8 ^e	1.4 ^d 1.3 ^e	N/A	N/A	N/A	N/A	N/A
Non-radiative rate constant, k_{nr} (10 ⁸ s ⁻¹)	5.1 ^d	4.4 ^d	6.5 ^d 6.3 ^e	3.5 ^d 3.3 ^e	N/A	N/A	N/A	N/A	N/A
Two-photon parameters									
Two-photon excitation maxima (nm)	1076, 1144	1060, 1120	1076, 1148	1060, 1124	1080, 1152	1048, 1116	~1070, ~1150	~1050, ~1110	N/A
Two-photon cross section, $\sigma_{2,A}$ (GM) ^f	25 (1060) 203 (740)	47 (1060) 154 (740)	35 (1080) 236 (740)	51 (1060) 125 (740)	28 (1080)	72 (1048)	24 (1072)	31 (1056)	N/A
Two-photon brightness, F ₂ (GM) ^{f,g}	1.0 (1060) 10 (740)	5.1 (1060) 17(740)	0.46 (1080) 3.1 (740)	9.3 (1060) 23 (740)	N/A	9.2 (1048)	0.21 (1072)	5 (1056)	N/A

N/A, not applicable. ND, not determined.

to L-lactate even at the highest concentration tested (Fig. 3a–d). R-eLACCO2 and R-eLACCO2.1 have in situ apparent $K_{d}s$ of 560 μ M and 5.1 mM for L-lactate, respectively (Fig. 3d). Similar to TTHA0766-based eLACCO2.1 (Ref. 20), R-eLACCO2 and R-eLACCO2.1 display Ca²+dependent fluorescence with apparent $K_{d}s$ of 310 μ M and 610 μ M, respectively (Fig. 3e). These in situ $K_{d}s$ are much lower than the extracellular Ca²+ concentration (1.5 – 1.7 mM) in brain²6. The bath application of 10 mM L-lactate revealed that R-eLACCO variants had an on rate (τ_{on}) of 61±5s and 61±3s for R-eLACCO2 and R-eLACCO2.1, respectively (mean ± s.d., Fig. 3f). The off rates (τ_{off}) of R-eLACCO2 and R-eLACCO2.1 are 72±4s and 35±3s, respectively (mean ± s.d., Fig. 3f).

Many cpmApple-based biosensors can undergo photoactivation when illuminated with blue light²⁵ and often display a complex photostability behavior compared to GFP²⁷. Blue-light illumination (-4 mW cm² at 470 nm) elicited a small increase in fluorescence intensity of the R-eLACCO variants expressed in HeLa cells (Fig. 3g). This result indicates that the photoactivation and recovery of the R-eLACCO variants occurs with far smaller $\Delta F/F$ (-0.02–0.05) and with much faster kinetics than L-lactate dependent fluorescence response (Fig. 3c,d,f). R-eLACCO2 and R-eLACCO2.1 expressed in HeLa cells showed higher photostability (integrated fluorescence, IF, of 1251 ± 18 and 1485 ± 32, mean ± s.d., respectively) than the parent mApple RFP

(IF of 848 ± 17 , mean \pm s.d.) in the absence of L-lactate, and lower photostability (IF of 702 ± 5 for R-eLACCO2 and 731 ± 9 for R-eLACCO2.1, mean \pm s.d.) in the presence of L-lactate (Fig. 3h, Supplementary Table 1). R-deLACCO_{ctrl} was more photostable than mApple in both the presence (IF of 1229 ± 4 , mean \pm s.d.) and absence (IF of 1250 ± 7 , mean \pm s.d.) of L-lactate.

To directly observe the spatiotemporal dynamics of L-lactate, we coexpressed R-eLACCO2.1 and iLACCO1 (Ref. 28) for extracellular and intracellular L-lactate imaging in starved glioblastoma cells (Fig. 3i). Glucose stimulation evoked concomitant fluorescence increases of both R-eLACCO2.1 and iLACCO1 (Fig. 3j,k). R-deLACCO_{ctrl} showed a decrease in fluorescence intensity, presumably due to a pH decrease concomitant with an L-lactate increase (Fig. 3k). We also observed HeLa cells expressing R-eLACCO2 in the presence of caged L-lactate (MNI-L-lactate) that releases L-lactate upon violet light illumination (Fig. 3l)²⁹. Upon 405-nm illumination, R-eLACCO2 showed a transient decrease presumably due to pH decrease by proton release, followed by an increase in its fluorescence intensity (Fig. 3m,n). R-deLACCO_{ctrl} showed a similar transient decrease in its fluorescence intensity but did not show substantial fluorescence response upon illumination. These results indicate that R-eLACCO2 variants can be used for extracellular

aCa²⁺

^bCalculated using the equation, $log_{10}([anionic]/[neutral]) = pH - pK_{ar}, where pH is 7.2 and pK_a is 7.69 (Ca²⁺ free) and 6.36 (Ca²⁺ bound).$

[°]Calculated using the equation, $log_{10}([anionic]/[neutral]) = pH - pK_a$, where pH is 7.2 and pK_a is 6.5.

dMeasured by C. Q. Vu and S. Arai at Kanazawa University.

^eMeasured by M. Drobizhev at Montana State University.

fPeak wavelength (nm) is represented in parentheses.

gTwo-photon brightness is presented as $F_2 = \rho_{\Delta} \times \sigma_{2,\Delta} \times \phi_{\Delta} + \rho_{N} \times \sigma_{2,N} \times \phi_{\Delta}$

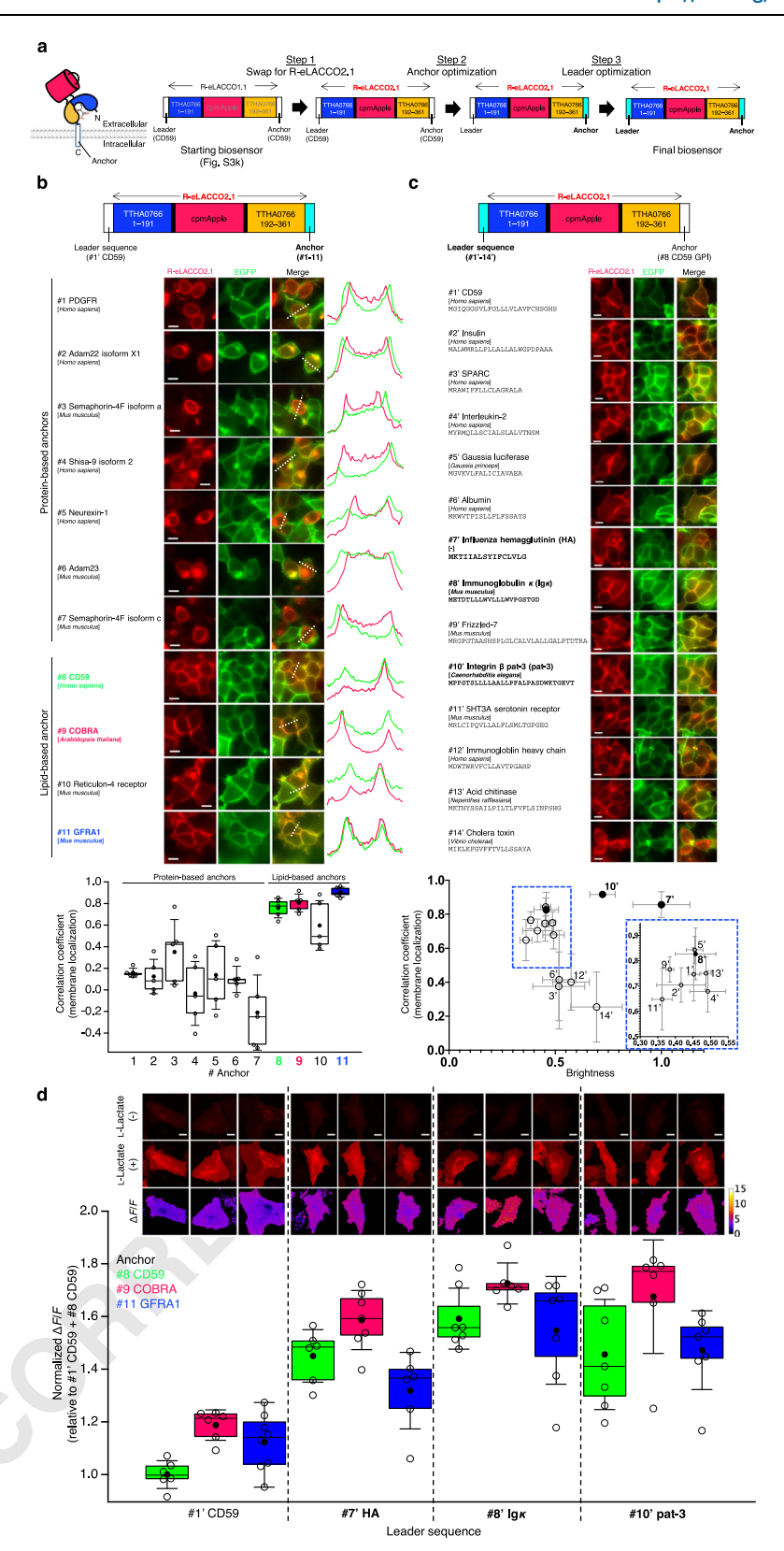
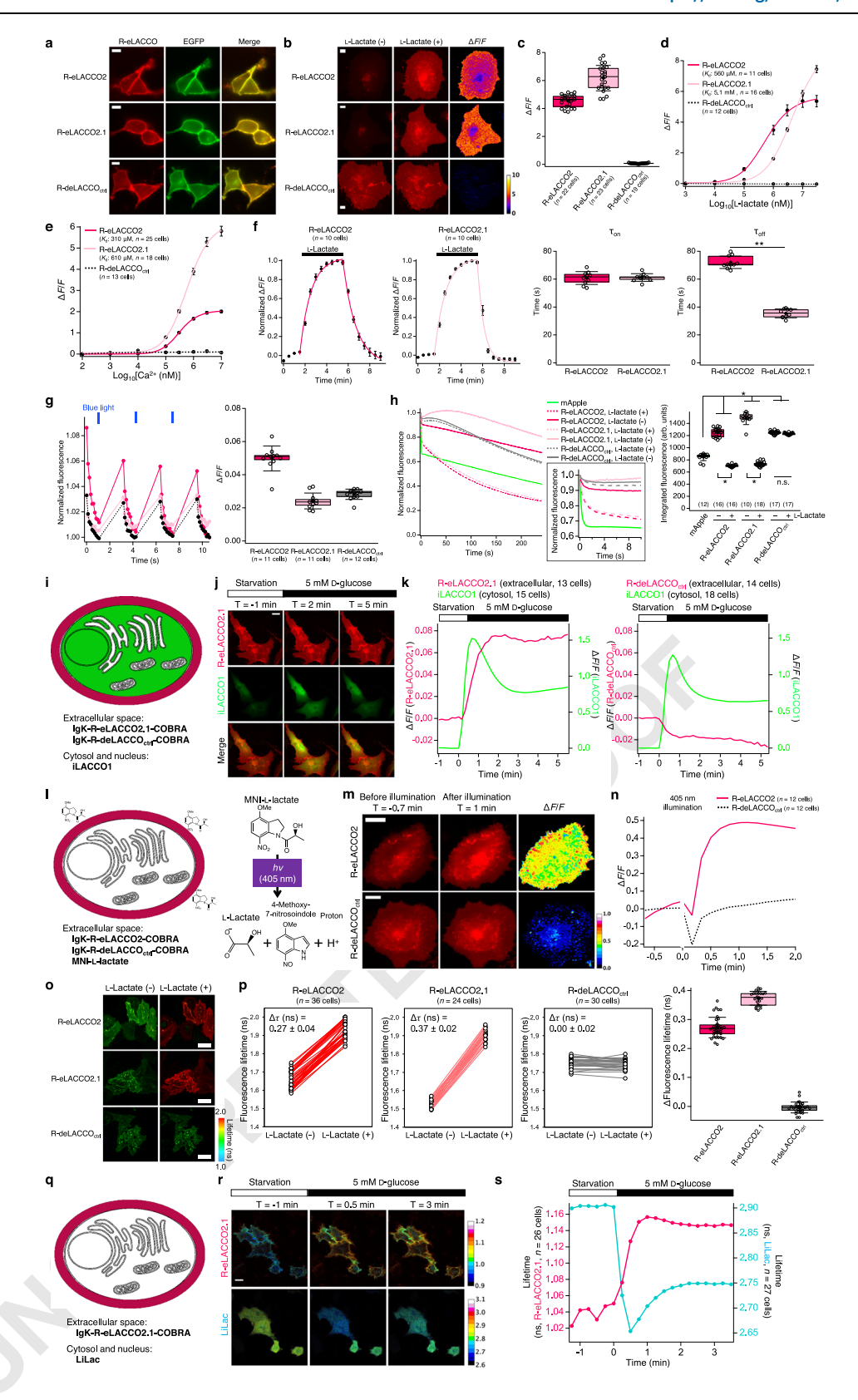


Fig. 2 | **Optimization of the extracellular membrane surface targeting.** a Overview of the biosensor optimization. **b** Localization of R-eLACCO2.1 with CD59 leader and a range of anchors in HEK293T cells. Line-scans (right) correspond to dashed white lines on the merged images. EGFP with CD59 leader and CD59 GPI anchor was used as a cell surface marker. n = 5 cells per construct for the correlation coefficient. Scale bars, 10 μm. **c** Localization of R-eLACCO2.1 with various leader

sequences and CD59 GPI anchor in HEK293T cells. EGFP with CD59 leader and CD59 GPI anchor was used as a cell surface marker. Mean \pm s.e.m., n = 4 cells per construct for correlation coefficient, n = 4 field of views (FOVs) per construct for brightness. Scale bars, 10 μ m. d Relative $\Delta F/F$ of R-eLACCO2.1 with a range of combinations of leader and anchor in HeLa cells. Scale bars, 20 μ m. Source data are provided as a Source Data file.



L-lactate imaging in combination with green fluorescent biosensors and violet-light activated molecular tools.

When using FLIM, the application of 10 mM L-lactate robustly increased fluorescence lifetime of R-eLACCO2 ($\Delta \tau$ of 0.27 \pm 0.04, mean \pm s.d.) and R-eLACCO2.1 ($\Delta \tau$ of 0.37 \pm 0.02, mean \pm s.d.) expressed on the surface of HeLa cells, while R-deLACCO_{ctrl} ($\Delta \tau$ of 0.00 \pm 0.02, mean \pm s.d.) did not respond to L-lactate (Fig. 3o,p). Glucose stimulation of

T98G cells co-expressing R-eLACCO2.1 and LiLac, a previously reported fluorescence lifetime biosensor for intracellular L-lactate²², resulted in the expected fluorescence lifetime increase of R-eLACCO2.1, concomitant with the expected fluorescence lifetime decrease of LiLac (Fig. 3q-s). These results indicate that R-eLACCO2 variants can also be used as FLIM biosensors for extracellular L-lactate in living cells.

Fig. 3 | Characterization of R-eLACCO2 variants in live mammalian cells.

a Localization of biosensors with leader (lgx) and anchor (COBRA) in HEK293T cells. EGFP with leader (CD59) and anchor (CD59) as a cell surface marker. Scale bars, 10 μ m. **b** Fluorescence images of R-eLACCO variants on HeLa cells before and after 10 mM L-lactate treatment. Scale bars, 10 μ m. **c** $\Delta F/F$ of R-eLACCO variants on HeLa cells. **d** L-Lactate titration of R-eLACCO variants on HeLa cells. Mean \pm s.e.m. **e** Ca²⁺ titration of R-eLACCO variants on HeLa cells in the presence (10 mM) of L-lactate. Mean \pm s.e.m. **f** Time course (left, mean \pm s.d.) and time constant (right) of the fluorescence response of R-eLACCO variants on HeLa cells upon L-lactate (10 mM) treatment. Two-tailed unpaired Student *t*-test. **p < 0.0001. **g** Fluorescence traces (mean \pm s.e.m.) and $\Delta F/F$ in response to blue light in HeLa cells expressing R-eLACCO variants. **h** Photobleaching curves (left, mean \pm s.e.m.) and integrated fluorescence (right) of R-eLACCO variants in the presence (10 mM) and absence of L-lactate on HeLa cells. Parentheses represent number of cells investigated. One-

way ANOVA followed by Tukey's multiple comparisons. *p< 0.0001. i Dual-color L-lactate imaging in extracellular space and cytosol. j Fluorescence images of cell surface-targeted R-eLACCO2.1 and cytosolic iLACCO1 expressed in T98G cells. Scale bar, 20 μ m. k Fluorescence traces for extracellular and cytosolic L-lactate in T98G cells upon glucose treatment. Mean \pm s.e.m. l L-Lactate imaging with MNI-L-lactate. m Fluorescence images of cell surface-targeted biosensors on HeLa cells before and after 405 nm light illumination. Scale bars, 20 μ m. n Fluorescence traces for extracellular L-lactate in HeLa cells upon a pulse of 405-nm light. Mean \pm s.e.m. o FLIM images of cell surface-targeted R-eLACCO2 variants on HeLa cells. Scale bars, 50 μ m. p Fluorescence lifetime change of R-eLACCO2 variants on HeLa cells. q FLIM imaging of L-lactate in extracellular space and cytosol. r FLIM images of cell surface-targeted R-eLACCO2.1 and cytosolic LiLac expressed in T98G cells. Scale bar, 20 μ m. s FLIM traces for extracellular and cytosolic L-lactate in T98G cells upon glucose treatment. Mean \pm s.e.m.

Validation of R-eLACCO2 variants in neural cells and suprachiasmatic nucleus slices

To characterize the performance of R-eLACCO variants on the surface of neurons, we expressed them under the control of a neuron-specific promoter, human synapsin (hSyn), in rat primary cortical neurons. We observed that neurons expressing R-eLACCO2 exhibited bright membrane-localized fluorescence (Fig. 4a). Upon bath application of 10 mM L-lactate, R-eLACCO2 and R-eLACCO2.1 had $\Delta F/F$ values of 4.3 ± 0.3 and 4.5 ± 0.2 (mean \pm s.e.m.), respectively, whereas R-deLACCO_{ctrl} had no response (Fig. 4b,c). The R-eLACCO biosensors under the control of an astrocyte-specific promoter gfaABC1D were also expressed correctly on the surface of rat primary cortical astrocytes (Fig. 4d). R-eLACCO2 and R-eLACCO2.1 displayed ΔF/F values of 4.7 ± 0.4 and 3.9 ± 0.4 (mean \pm s.e.m., Fig. 4e,f), respectively, upon bath application of 10 mM L-lactate. R-deLACCO_{ctrl} showed no response to L-lactate, similar to our results obtained with HeLa cells and neurons. We determined that the R-eLACCO biosensor was sufficiently robust and user-friendly, as shown by an independent laboratory (Supplementary Fig. 9).

To determine whether R-eLACCO2.1 could be used to detect changes in L-lactate concentration in intact tissue, we examined suprachiasmatic nucleus (SCN) slices prepared from mice brains and transduced with an adeno-associated virus (AAV) encoding R-eLACCO2.1 under hSyn promoter (Fig. 4g). Although the high glucose concentration (15 mM) in the medium could elevate basal extracellular L-lactate level, bath application of L-lactate elicited a significant increase in R-eLACCO2.1 fluorescence compared to R-deLACCO_{ctrl} at all doses tested: 10 mM ($\Delta F/F = 0.67 \pm 0.18$ vs. 0.12 ± 0.05 , mean \pm s.e.m.) and 40 mM ($\Delta F/F = 1.37 \pm 0.24$ vs. -0.04 ± 0.01 , mean \pm s.e.m.) (Fig. 4h–j). Taken together, these results indicated that R-eLACCO variants with the optimized leader and anchor can be used for imaging of extracellular L-lactate on the surfaces of cultured neurons and astrocytes, and brain slices.

In vivo validation in awake mice

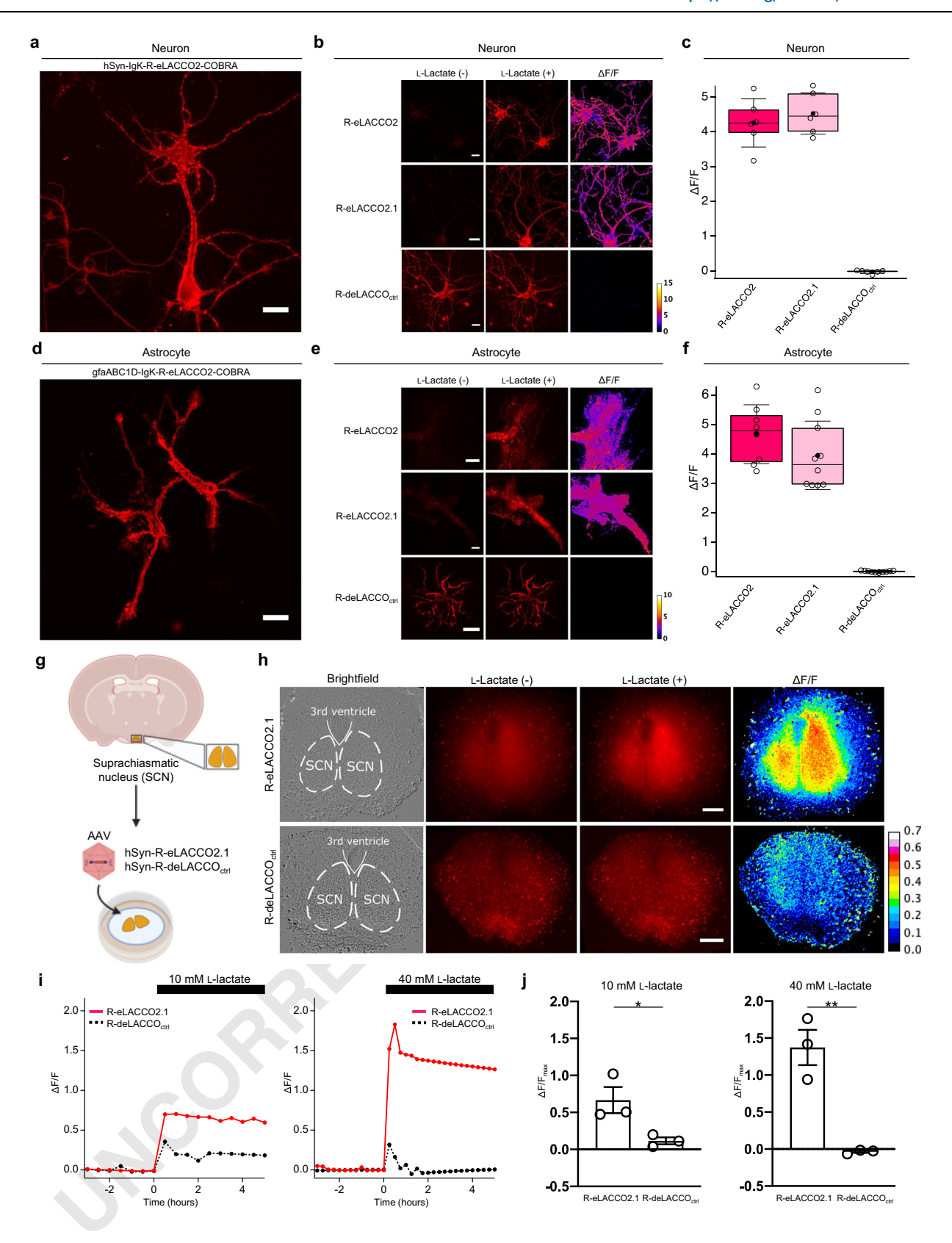
To validate the performance of R-eLACCO2.1 in vivo, we expressed R-eLACCO2.1 in the primary vibrissa somatosensory (vS1) cortex of adult mice by injecting an AAV encoding hSyn-R-eLACCO2.1 (Fig. 5a). L-Lactate, when injected intravenously, can cross the blood-brain barrier to reach neurons in the brain. Upon intravenous (i.v.) injection of L-lactate via a tail vein of an awake mouse as a representative trial, R-eLACCO2.1 showed a robust fluorescence increase at the depths of 100 µm and 400 µm under two-photon laser scanning microscopy implemented with adaptive optics (AO2P) (Fig. 5b). To further confirm whether R-eLACCO2.1 monitors extracellular L-lactate dynamics in mice, we separately recorded the fluorescence signal of R-eLACCO2.1 and the electric signal of an electrochemical (EC) L-lactate probe that was calibrated in vitro and implanted in vS1 (Fig. 5c). The EC probe and R-eLACCO2.1 showed the lactate-dependent signal increase

decrease, whereas R-deLACCO_{ctrl} showed virtually no change in fluorescence intensity at all doses investigated (Fig. 5d). Saline injection also resulted in a small fluorescence response in R-eLACCO2.1 for reasons that remain unclear (Fig. 5d and Supplementary Fig. 10a). This imaging revealed the high correlation between the signals of R-eLACCO2.1 and EC lactate probe (Fig. 5e), thereby confirming the functionality of R-eLACCO2.1 as a biosensor for extracellular L-lactate. R-eLACCO2.1 exhibits a higher fluorescence response than GFP-based extracellular L-lactate biosensor eLACCO2.1 (Ref. 20) in live mice imaging upon i.v. injection of L-lactate (Fig. 5f). These results indicate that R-eLACCO2.1 is well functional as an extracellular L-lactate biosensor in vivo.

Multiplexed in vivo L-lactate imaging

To monitor endogenous extracellular L-lactate dynamics in awake mice, we expressed R-eLACCO2.1 in vS1 neurons and recorded its fluorescence response and the locomotion velocity in response to airpuff vibrissae stimulation (Fig. 6a). In vS1 layer II/III neurons, stimulation of the vibrissae increased not only the fluorescence intensity of R-eLACCO2.1 but also locomotion (Fig. 6b). Long-term imaging under consistent conditions demonstrates that the fluorescence intensity of R-eLACCO2.1 remains relatively stable (Supplementary Fig. 10b), suggesting that the observed decrease in fluorescence is predominantly driven by changes in extracellular lactate concentration, rather than by photobleaching. Spontaneous locomotion following a 30-second rest period resulted in a comparable increase in R-eLACCO2.1's fluorescence intensity to that observed during a 20-second vibrissa stimulation (Fig. 6c), suggesting that the observed fluorescence response in vibrissae-stimulated mice primarily results from locomotion. Whisker stimulation that does not induce locomotion shows minimal fluorescence response (Supplementary Fig. 10c), supporting the premise that the broad variability among individual measurements is primarily due to inherent biological variability and behavioral responses to stimuli. Note that vibrissa stimulation induces vasodilation and functional hyperemia in mice, which in turn leads to a decrease in the measured fluorescence intensity of biosensors due to increased absorption of the excitation and emission light (Fig. 6b,c and Supplementary Fig. 10d,e). In contrast, R-deLACCO_{ctrl} exhibited negligible change in fluorescence intensity upon either vibrissae stimulation or locomotion (Fig. 6c and Supplementary Fig. 10f-h). In vivo imaging further confirmed that R-eLACCO2.1 can detect reductions in extracellular lactate levels returning to the basal level during periods of rest following locomotion, as illustrated in Supplementary Fig. 10i. These findings confirm that R-eLACCO2.1 can detect the dynamics of endogenous extracellular L-lactate in awake mice with cellular resolution.

Finally, we investigated the interplay between neural activity and metabolism in awake mice by employing multiplexed AO2P imaging. For this purpose, we injected an AAV mixture containing hSyn-ReLACCO2.1 and hSyn-cre into transgenic mice, which conditionally



express the intracellular Ca²⁺ biosensor GCaMP6f in neuronal populations (Fig. 6d)²⁴. Both one-photon wide-field imaging and AO2P imaging revealed the localization of R-eLACCO2.1 at the cell surface and GCaMP6f within the cell bodies, excluding the nuclei in a selection of layer II/III neurons within the vS1 region, confirming in vivo expression (Fig. 6e). In trials without major locomotion events, we observed that spontaneous neuronal activations were succeeded by a gradual

reduction and subsequent restoration of extracellular L-lactate levels (Fig. 6f,g, Supplementary Fig. 10j). R-deLACCO_{ctrl} did not show such transient decrease in its fluorescence upon spontaneous neuronal activations and only show a signal increase due to bleedthrough of GCaMP6f's signal. Collectively, these results demonstrate the utility of R-eLACCO2.1 for the concurrent monitoring of both the dynamics of endogenous extracellular L-lactate and neural activities in awake mice.

Fig. 4 | Validation of R-eLACCO2 variants in brain cells and tissues.

a Fluorescence images of primary cultured rat cortical neurons expressing R-eLACCO2. Scale bar, 20 μm. **b** Fluorescence images of R-eLACCO variants expressed on cell surface of rat cortical neurons before and after 10 mM L-lactate stimulation. Scale bars, 20 μm. **c** L-Lactate-dependent $\Delta F/F$ of R-eLACCO variants expressed on primary neurons. n = 6 FOVs over 6 wells per construct. **d** Fluorescence images of primary cultured rat cortical astrocytes expressing R-eLACCO2. Scale bar, 20 μm. **e** Fluorescence images of R-eLACCO variants expressed on the cell surface of rat cortical astrocytes before and after 10 mM L-lactate stimulation. Scale bars, 20 μm. **f** L-Lactate-dependent $\Delta F/F$ of R-eLACCO variants expressed on primary astrocytes. n = 8, 8, and 10 cells for R-eLACCO2, R-LACCO2.1, and R-deLACCO_{ctrl}, respectively. Mean \pm s.e.m. **g** Schematic showing

transduction of organotypic coronal slices of the suprachiasmatic nucleus (SCN). This graphic was created with Biorender.com. **h** Fluorescence images of the SCN slices expressing hSyn-R-eLACCO2.1 or hSyn-R-deLACCO_{ctrl}. First columns show fluorescence signals with brightfield, indicating location of the SCN and 3^{rd} ventricle in white. Scale bars, 200 µm. **i** Fluorescence intensity timeseries of hSyn-R-eLACCO2.1 and hSyn-R-deLACCO_{ctrl} in the whole SCN regions (**h**) before and after addition of 10 mM (left) or 40 mM (right) L-lactate to medium. Each dot represents a datapoint. Mean \pm s.e.m., n = 3 slices from 3 mice per biosensor. **j**) $\Delta F/F_{\rm max}$ of each biosensor treated with 10 mM (left) or 40 mM (right) L-lactate. Mean \pm s.e.m., n = 3 slices from 3 mice per biosensor. One-sided Welch's unpaired t-test, *p = 0.0406, **p = 0.0135. Source data are provided as a Source Data file.

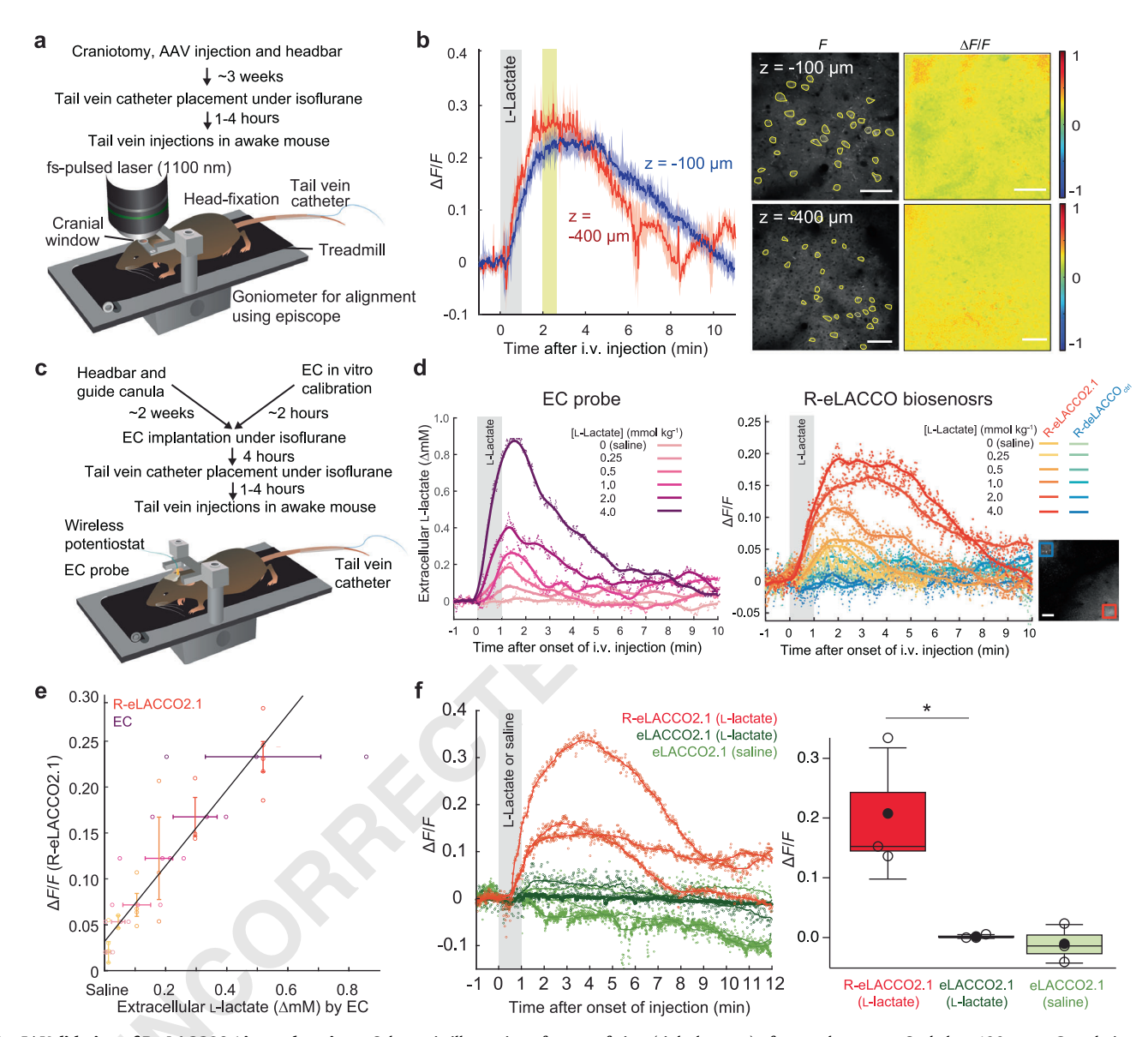


Fig. 5 | **Validation of R-eLACCO2.1 in awake mice. a** Schematic illustration of in vivo mouse imaging upon i.v. L-lactate injection. **b** Fluorescence response traces (left) of the primary vibrissa somatosensory (vS1) cortex in an awake mouse expressing hSyn-R-eLACCO2.1 upon i.v. injection of L-lactate (4 mmol kg¹). Mean \pm s.d. (n = 30 neurons). The right panels show representative images of F and $\Delta F/F$ at the time marked in yellow. Scale bars, 100 μm. **c** Schematic illustration of in vivo imaging for a calibrated EC L-lactate probe in awake mice. **d** Signal traces of EC L-lactate probe (left), and R-eLACCO2.1 and R-deLACCO_{ctrl} (right) using AO2P. hSyn-R-eLACCO2.1 and hSyn-R-deLACCO_{ctrl} were simultaneously recorded in a field

of view (right bottom) of an awake mouse. Scale bar, 100 μ m. $\bf e$ Correlation plot between the signals of R-eLACCO2.1 (4 mice) and EC probe (3 mice) in awake mice upon i.v. injection of L-lactate. Mean \pm s.d. The linear fit is overlaid with a slope of 0.41, an intercept of 0.03, and an R^2 of 0.9. $\bf f$ Fluorescence response traces of the layer I cortex in awake mice expressing hSyn-R-eLACCO2.1 (excited at 1,100 nm) or hSyn-eLACCO2.1 (excited at 930 nm) upon i.v. injection of L-lactate (4 mmol kg⁻¹) or saline using AO2P (3 mice for each biosensor). Two-sided ANOVA with Dunnett's post hoc tests. *p = 0.0206. Source data are provided as a Source Data file.

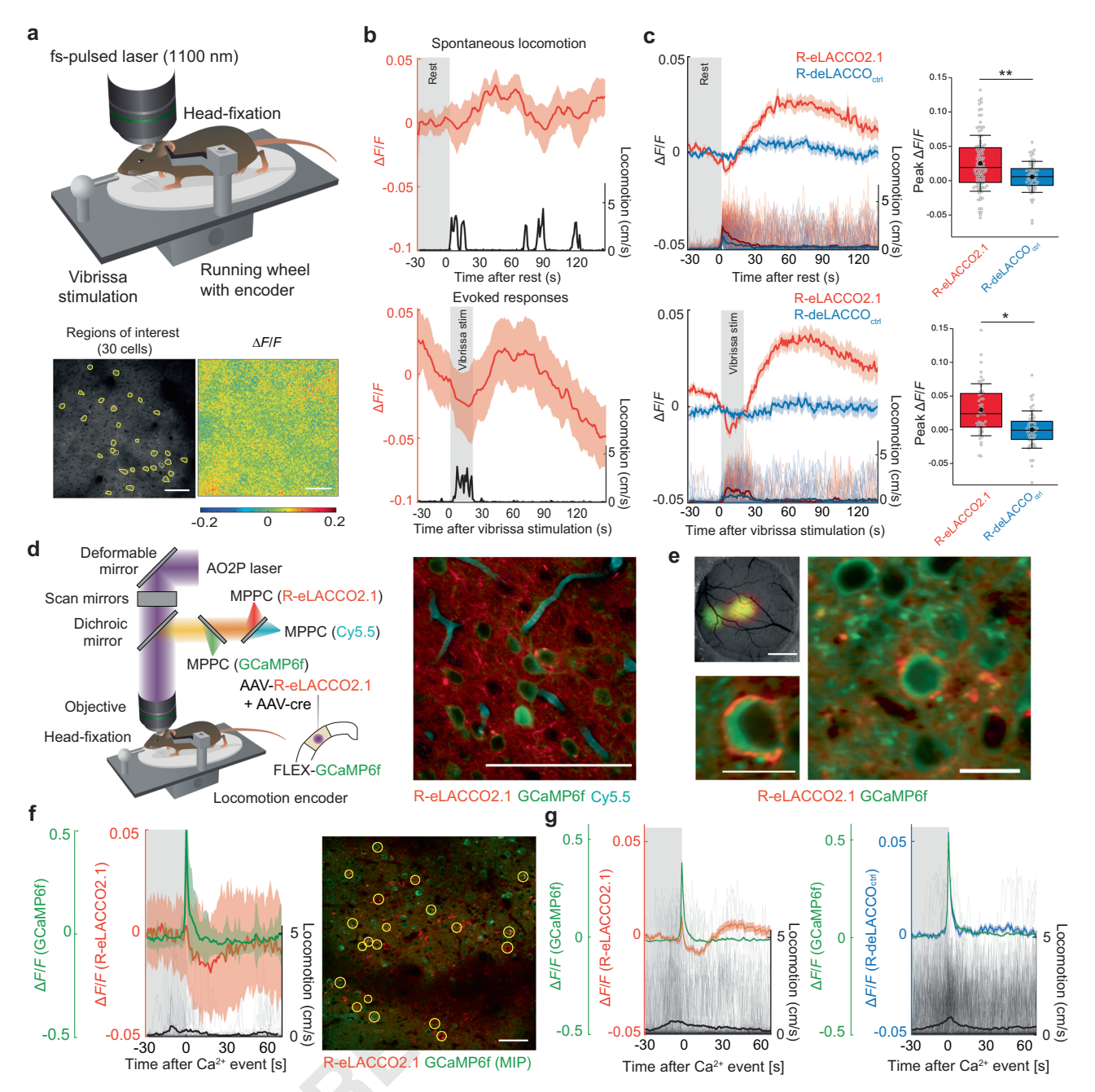


Fig. 6 | **In vivo L-lactate dynamics during neural activity. a** The setup for recording of R-eLACCO2.1 and locomotion in an awake mouse under air-puff stimulation (20 s of 4 Hz) to multiple vibrissae. $\Delta F/F$ map (bottom) of the same field of view averaged for 60–80 s after a vibrissa stimulation onset. Scale bars, 100 μm. **b** $\Delta F/F$ traces of R-eLACCO2.1 under air-puff stimulation and spontaneous locomotion after 30 s rest in an example mouse (mean ± s.d. of the 30 cells indicated in panel **a**). **c** Averaged $\Delta F/F$ traces of hSyn-R-eLACCO2.1 (n = 107 locomotion events, n = 48 vibrissae stimulations in 5 mice) and hSyn-R-deLACCO_{ctrl} (n = 59 locomotion events, n = 53 vibrissae stimulations in 3 mice) under spontaneous locomotion following 30-s rest (upper) and air-puff stimulation (bottom). Mean ± s.e.m. Two-tailed Welch's unpaired t-test. **p = 0.0001 (locomotion events), *p < 0.0001 (vibrissae stimulation). **d** Schematic illustration of simultaneous imaging of L-lactate and Ca²⁺ in awake mice under AO2P. Mice co-expressing R-eLACCO2.1 (red, excited at 1,030 nm) and GCaMP6f (green, excited at 1,030 nm) in v\$1 neurons

were i.v. injected with Cy5.5 dye (vasculature, cyan, excited at 950 nm). Scale bar, $100 \, \mu m$. **e** Verification of R-eLACCO2.1 and GCaMP6f expression in one-photon widefield imaging (left top, scale bar $100 \, \mu m$) and AO2P imaging (left bottom and right, scale bars $20 \, \mu m$). **f** Representative $\Delta F/F$ traces of neurons co-expressing R-eLACCO2.1 and GCaMP6f in an awake mouse identified on a maximum intensity projection. n=20 neurons and $46 \, \text{Ca}^{2+}$ events after 30 seconds of quiescence from one mouse. Mean \pm s.d. Scale bar, $20 \, \mu m$. **g** $\Delta F/F$ traces of neurons co-expressing GCaMP6f and R-eLACCO2.1 (left, n=80 neurons and $247 \, \text{Ca}^{2+}$ events after $30 \, \text{seconds}$ of quiescence from 4 mice) or R-deLACCO $_{\text{ctrl}}$ (right, $n=188 \, \text{neurons}$ and $478 \, \text{Ca}^{2+}$ events after $30 \, \text{seconds}$ of quiescence from 3 mice) in awake mice. Mean \pm s.e.m. The increases in fluorescence observed for both R-eLACCO2.1 and R-deLACCO $_{\text{ctrl}}$ at t=0 are attributable to bleedthrough from the GCaMP6f signal. Source data are provided as a Source Data file.

Discussion

An emerging appreciation of the intercellular shuttling of L-lactate, with important roles in both energetics and signaling, has highlighted the need for improved methods to visualize extracellular L-lactate. To

broaden the range of possibilities for multiplexed imaging, we have now expanded the color spectrum of the eLACCO family^{20,23} by engineering a red fluorescent biosensor, R-eLACCO2.1. In addition to its inherent advantage over enzyme-mediated electrochemical probes

that are invasive and do not provide high-resolution spatial information¹², and its inherent advantage of being spectrally orthogonal to GCaMP variants. R-eLACCO2.1 is more sensitive to extracellular L-lactate increases than green fluorescent eLACCO2.1 in vivo. Indeed, we have observed dynamic changes in the concentration of extracellular L-lactate in the vS1 cortex of awake mice expressing R-eLACCO2.1 upon spontaneous locomotion at the cellular resolution. We simultaneously recorded signals of R-eLACCO2.1 and GCaMP6f in awake mice and found that the concentration of extracellular L-lactate transiently decreases upon neural activities. Moreover, R-eLACCO2.1 also serves as a FLIM biosensor that is robust to changes in its expression level, excitation power, and focus drift³⁰. Overall, R-eLACCO2.1 is a red fluorescent biosensor for minimally invasive imaging of the dynamics of extracellular L-lactate with cellular resolution, enabling an orthogonal readout of distinct and multiple events in cellular metabolism and activity.

To the best of our knowledge, R-eLACCO2 is a first-in-class red fluorescent extracellular L-lactate biosensor that enables multiplexed imaging with commonly used optical biosensors and actuators in live samples. However, there are several important considerations that users should pay close attention to. As with eLACCO2.1, the TTHA0766-based R-eLACCO2 only functions as an L-lactate biosensor in the presence of Ca²⁺. For extracellular applications, this should not be a major concern because the apparent K_d s of R-eLACCO2 (310 μ M) and R-eLACCO2.1 (610 µM) for Ca²⁺ are substantially lower than the physiological and pathological Ca²⁺ concentration range (-1.5–1.7 mM) in the extracellular space of brain tissue²⁶. However, given that the Ca²⁺ concentration in the extracellular environment can transiently decrease to ~1 mM during neural activity artificially evoked by extreme stimulations such as long trains of action potentials³¹, careful consideration should be taken when interpreting the fluorescence signal of R-eLACCO2 variants in brain tissue. A change in extracellular Ca²⁺ concentration from 1.7 mM to 1.0 mM could cause up to a -8.6% or -15% fluorescence intensity change for R-eLACCO2 and R-eLACCO2.1 respectively. Furthermore, variations in extracellular Ca²⁺ concentration can alter the apparent K_d of the biosensor for L-lactate. Another important consideration for the application of R-eLACCO2 is the kinetics of fluorescence response. R-eLACCO2 variants, similar to eLACCO2.1, show relatively slow kinetics of fluorescence turn-on response compared to GCaMP²⁴ and R-GECO1 (Ref. 32). Previous work using enzyme-mediated electrodes has revealed that the concentration of L-lactate in the extracellular space typically changes on the time scale of a dozen of seconds to minutes in brain tissue¹². As lactate dynamics are much slower than neural activity-dependent intracellular Ca²⁺ dynamics (-ms to s), R-eLACCO2 variants are likely to be well-suited for investigating physiologically relevant changes in the extracellular L-lactate concentration in brain tissue. A final important consideration is the ability to detect decreases in extracellular L-lactate below baseline levels. While our in vitro and in vivo characterizations demonstrate the biosensor's sensitivity to reductions in L-lactate, caution should be exercised when interpreting fluorescence decreases below the physiological baseline.

Genetically encoded fluorescent biosensors for extracellular targets have generally used periplasmic binding proteins (PBPs, e.g., LACCO sensors^{20,23}, SnFR sensors^{33,34}) or G-protein-coupled receptors (GPCRs, e.g., GRAB sensors^{35,36}, Light sensors^{37,38}) as the target sensing domain. Membranous GPCR-based biosensors intrinsically express on cell membrane, whereas soluble PBP-based biosensors require to fuse N-terminal leader and C-terminal anchor domain for their expression on cell membrane. We previously revealed that the specific choice of leader and anchor domain is of critical importance in the biosensor performance^{20,23}. In this study, we first optimized the efficiency of membrane localization of the biosensor using HEK293T cells which have a clear membrane structure, followed by the optimization of $\Delta F/F$ using HeLa cells which have a flat cell morphology. These screenings

identified Igx and COBRA as the best leader and anchor domains, respectively, for R-eLACCO2.1. In the previous study²⁰, the best leader/ anchor combination of eLACCO2.1 has been identified as HA (Influenza hemagglutinin) and NGR (reticulon-4 receptor), respectively, based on the neuron-based screening similar to this study. These results suggest the best leader/anchor combination depends on the specific biosensor and the screening method. Consistent with our previous works^{20,23}, the present study suggests that lipid-based GPI anchors generally provide better biosensor performance than protein-based anchors. In addition, the N-terminal leader sequences of the biosensor have a substantial impact on their membrane localization efficiency, $\Delta F/F$, and expression level. Considering that $\Delta F/F$ (= 6.5) of R-eLACCO2.1 in HeLa cells is much smaller than that (= 12) in vitro, it might be possible that screening of a combinatorial library of leader and anchor might provide further improvement in $\Delta F/F$ in living cells. Application of the leader-anchor optimization strategy to non-TTHA0766-based biosensors, such as R-iLACCO1 (Ref. 20) and FiLa-Red21, might yield alternative red fluorescent extracellular L-lactate biosensors with Ca2+ insensitivity.

L-Lactate dynamics in living mice brain have been previously investigated under anesthesia conditions⁶. In this study, we observed relatively slow transients in extracellular L-lactate following episodes of increases in locomotion and pupil diameters in the vS1 cortex of awake mice. These transients resembled the response patterns of neuromodulators such as norepinephrine that is known to induce aerobic glycolysis, rather than those of synapse-localized neurotransmitters like glutamate^{39,40}. These observations are consistent with extracellular L-lactate serving as a neuromodulator-like metabolite or a signaling molecule through broadly expressed receptors such as HCA1 (GPR81) or monocarboxylate transporters (MCTs), potentially influencing ATP/ADP ratios or redox states41-43. Previous works using ¹H-NMR spectroscopy that demonstrate an L-lactate increase in the cortex of humans or rats upon stimulations also align with the present study⁴⁴⁻⁴⁶. Interestingly, multiplexed in vivo imaging of R-eLACCO2.1 and GCaMP6f did not indicate an increase in extracellular L-lactate concentration following neuronal activity. This observation suggests localized L-lactate consumption or evacuation into bloodstream rather than cellular L-lactate export induced by local neural activity, even though these findings do not directly resolve the ANLS hypothesis^{5,6,11}. These observations are largely consistent with reported in vivo electrical stimulations resulting in initial decreases of extracellular and astrocytic L-lactate followed by a larger delayed increase depending on the stimulation strength⁴⁷. Future work should differentiate the activity of local neurons and associated neuromodulation effects when reporting stimulation-induced L-lactate or NADH transients and consider the effects of local oxygen and NADH availability^{11,48}.

In summary, this study describes the development of a red fluorescent genetically encoded extracellular L-lactate biosensor, designated R-eLACCO2.1. Extensive directed evolution and site-directed mutagenesis followed by an intensive effort to optimize the combination of leader and anchor domain for targeting to the extracellular environment ultimately led to the R-eLACCO biosensors that enable extracellular L-lactate imaging in vitro, ex vivo, and in vivo with high sensitivity. The high-performance L-lactate biosensor introduced here should provide new opportunities to investigate the emerging roles of L-lactate, including the controversial ANLS hypothesis, particularly in the context of multiplexed imaging with green fluorescent biosensors.

Methods

General methods and materials

The gene encoding the lactate binding bacterial periplasmic protein TTHA0766 was derived from the gene encoding the previously reported L-lactate biosensor eLACC01 (Ref. 23). The gene encoding cpmApple was derived from the gene encoding the previously

reported Ca²⁺ biosensor R-GECO1 (Ref. 32). Phusion high-fidelity DNA polymerase (Thermo Fisher Scientific) was used for routine polymerase chain reaction (PCR) amplifications, and Taq DNA polymerase (New England Biolabs) was used for error-prone PCR. Q5 high-fidelity DNA polymerase (New England Biolabs) was used for site-directed mutagenesis⁴⁹. Restriction endonucleases, rapid DNA ligation kits, and GeneJET miniprep kits were purchased from Thermo Fisher Scientific. PCR products and products of restriction digests were purified using agarose gel electrophoresis and the GeneJET gel extraction kit (Thermo Fisher Scientific). DNA sequences were analyzed by DNA sequence service of Fasmac Co., Ltd. Fluorescence excitation and emission spectra were recorded on a Spark plate reader (Tecan).

Engineering of R-eLACCO2

The gene encoding cpmApple with N- and C- terminal linkers (DW and EADG, respectively) was amplified using the R-GECO1 gene as a template, followed by insertion between the codons encoding Ile191 and Gly192 of TTHA0766 in pBAD-eLACCO1 (Ref. 23) by Gibson assembly (New England Biolabs). The resulting variant, designated R-eLACCOO.1, was subjected to an iterative process of library generation and screening in E. coli strain DH10B (Thermo Fisher Scientific) in LB media supplemented with 100 µg mL⁻¹ ampicillin and 0.02% L-arabinose. Libraries were generated by site-directed random mutagenesis or error-prone PCR of the whole gene. In the screening, proteins were extracted using B-PER bacterial protein extraction reagent (Thermo Fisher Scientific) and tested for fluorescence brightness and lactate-dependent response. For each round, approximately 100-400 fluorescent colonies were picked, cultured, and tested on 96-well plates under a plate reader. There were 22 rounds of screening and one site-directed mutagenesis (Ile191Val) before R-eLACCO2 was identified. Leu79Ile mutation was added to R-eLACCO2 to tune the lactate affinity by extending the R-eLACCO2 template using Q5 high-fidelity DNA polymerase and oligonucleotides containing Leu79Ile mutation (CTG to ATC) followed by digestion with DpnI (Thermo Fisher Scientific). The resulting low-affinity mutant was designated R-eLACCO2.1. Asp441Asn mutation was added to R-eLACCO2 to abrogate the lactate affinity. Six rounds of directed evolution were performed to improve the brightness of R-eLACCO2 Asp441Asn. The resulting mutant was designated as R-deLACCO_{ctrl}.

Protein purification and in vitro characterization

The gene encoding R-eLACCO variants, with a poly-histidine tag on the N-terminus, was expressed from the pBAD vector. Bacteria were lysed with a sonicator (Branson) and then centrifuged at 15,000 g for 20 min, and proteins were purified by Ni-NTA affinity chromatography (Agarose Bead Technologies). Absorption spectra of the samples were collected with a Lambda950 Spectrophotometer (PerkinElmer) and UV-1800 Spectrophotometer (Shimadzu). To perform pH titrations, protein solutions were diluted into buffers (pH from 4 to 11) containing 30 mM trisodium citrate, 30 mM sodium borate, 30 mM MOPS, 100 mM KCl, 1 mM CaCl₂, and either no L-lactate or 100 mM L-lactate. Fluorescence intensities as a function of pH were then fitted by a sigmoidal binding function to determine the pK_a . For lactate titration, buffers were prepared by mixing an L-lactate (-) buffer (30 mM MOPS, 100 mM KCl, 1 mM CaCl₂, pH 7.2) and an L-lactate (+) buffer (30 mM MOPS, 100 mM KCl, 1 mM CaCl₂, 100 mM L-lactate, pH 7.2) to provide L-lactate concentrations ranging from 0 mM to 100 mM at 25 °C. Fluorescence intensities were plotted against L-lactate concentrations and fitted by a sigmoidal binding function to determine the Hill coefficient and apparent K_d . For Ca^{2+} titration, buffers were prepared by mixing a Ca²⁺ (-) buffer (30 mM MOPS, 100 mM KCl, 10 mM EGTA, 100 mM L-lactate, pH 7.2) and a Ca²⁺ (+) buffer (30 mM MOPS, 100 mM KCl, 10 mM CaEGTA, 100 mM L-lactate, pH 7.2) to provide Ca²⁺ concentrations ranging from 0 µM to 39 µM at 25 °C. Buffers with Ca²⁺ concentrations more than 39 μM were prepared by mixing a Ca²⁺ (-, w/ o EGTA) buffer (30 mM MOPS, 100 mM KCl, 100 mM L-lactate, pH 7.2) and a Ca^{2+} (+, w/o EGTA) buffer (30 mM MOPS, 100 mM KCl, 100 mM CaCl₂, 100 mM L-lactate, pH 7.2).

To collect the two-photon absorption spectra, the tunable femtosecond laser InSight DeepSee (Spectra-Physics, Milpitas, CA) was used to excite the fluorescence of the sample contained within a PC1 Spectrofluorometer (ISS, Champaign, IL)50. To measure the twophoton excitation spectral shapes, we used short-pass filters 633SP and 770SP in the emission channel. LDS 798 and Coumarin 540 A were used as spectral standards. Quadratic power dependence of fluorescence intensity in the proteins and standards was checked at several wavelengths across the spectrum. The two-photon cross section (σ_2) of the anionic form of the chromophore was measured⁵¹. Rhodamine 6 G in methanol was used as a reference standard with excitation at 1060 nm (Ref. 50). Extinction coefficients were determined by alkaline denaturation⁵². The two-photon absorption spectra were normalized to the measured σ_2 values. To normalize to the total two-photon brightness (F_2) , the spectra were then multiplied by the quantum yield and the relative fraction of the respective form of the chromophore for which the σ_2 was measured. The data is presented this way because R-eLACCO1.1 and R-eLACCO2 contain a mixture of the neutral and anionic forms of the cpmApple chromophore^{52,53}.

Transient absorption spectra of purified R-eLACCO2 protein in the presence (10 mM) and absence of L-lactate were measured by a femtosecond pump-probe method. The light source was a regenerative amplified mode-locked Ti:sapphire laser (Solstice, Spectra-Physics). The second harmonic was used for the excitation pulse. The probe light was a femtosecond supercontinuum generated by focusing a 1.3-µm signal light generated by an optical parametric amplifier (OPA) (TOPAS, Light Conversion Ltd.) onto a CaF₂ plate. The probe light was detected by a CMOS detector (Orca-Quest, Hamamatsu Photonics). Samples were measured with stirring using a glass cell with an optical path length of 2 mm.

Cryo-electron microscopy (cryo-EM) of R-eLACCO2

R-eLACCO2 in the lactate-bound state was prepared for cryo-EM analysis according to the following procedure. Equilibrated with buffer (20 mM Tris-HCl, pH 8.0, 150 mM NaCl, 1 mM CaCl₂), R-eLACCO2 protein was purified using a Superdex 200 Increase 10/300 GL column (GE Healthcare). The purified protein (final concentration of 0.2 mg mL⁻¹) in the presence of 10 mM L-lactate was applied to freshly glow-discharged Au 300 mesh R1.2/1.3 grids (Quantifoil) after adding 3 μL of amylamine, using a Vitrobot Mark IV (Thermo Fisher Scientific) at 6 °C, with a waiting time of 10 s and a blotting time of 4 s under 100% humidity conditions. The grids were then plunge-frozen in liquid ethane and cooled by liquid nitrogen. Cryo-EM data were collected using a Krios G3i microscope (Thermo Fisher Scientific) equipped with a Gatan BioQuantum Energy Filter and a Gatan K3 direct electron detector in the electron counting mode (The University of Tokyo, Japan) at 300 kV. Movies were recorded in a correlated double sampling (CDS) mode, at a nominal magnification of 105,000×, corresponding to a calibrated pixel size of 0.83 Å, with a total dose of approximately 50 electrons per Å² per 48 frames. The data were automatically acquired using the EPU software (Thermo Fisher Scientific), with a defocus range of -0.6 to -1.6 µm, and 8250 movies were obtained.

The data processing was performed with the cryoSPARC v4.4.0 software⁵⁴. The dose-fractionated movies were aligned using patch-based motion correction, and the contrast transfer function (CTF) parameters were determined using the patch-based CTF estimation. From the 8250 motion-corrected and dose-weighted micrographs, 5,862,141 particles were automatically picked and subjected to reference-free two-dimensional classifications. The particles were curated by cryoSPARC heterogenous refinement, using the maps derived from the cryoSPARC ab initio reconstruction as templates. The

selected particles were subjected to a three-dimensional classification, and the best two classes containing 297,990 particles were refined using non-uniform refinement⁵⁵ with optimization of the CTF value in C2 symmetry, yielding a map at 2.7 Å resolution, according to the Fourier shell correlation (FSC) of 0.143 criterion⁵⁶. This map showed the dimeric core of the TTHA0766 lactate-binding domain, but the cpmApple domains were not clearly visible. After reference-based motion correction and non-uniform refinement with C2 symmetry, the particles were expanded using C2 symmetry. A focused mask of one protomer was applied for the following three-dimensional classification without alignment and local refinement. The best reconstruction with 2.7 Å resolution from 146,454 particles showed the density of the cpmApple domain and linkers between TTHA0766 and cpmApple domains.

The model of TTHA0766 and cpmApple domains was built using the crystal structure of eLACCO1 (PDB 7E9Y)²³ and R-GECO1 (PDB 4I2Y)²⁵, respectively, followed by manual model building with COOT⁵⁷. The model was refined using REFMAC5 in the Servalcat pipeline⁵⁸, with secondary structure restraints prepared by ProSMART⁵⁹. The structure validation was performed using MolProbity⁶⁰. The statistics of the three-dimensional reconstruction and model refinement are summarized in Supplementary Table 2. The cryo-EM density map figures were generated using UCSF ChimeraX⁶¹.

Modeling and molecular dynamics (MD) simulations

All MD simulations, both apo and holo, were performed using Desmond⁶²/Maestro academic/non-commercial version 2023.4 (Desmond v7.6, mmshare v6.4, Maestro v13.8) with the OPLS 2005 force field^{63,64}. Simulations and analyses were conducted on an NVIDIA RTX 3080 Ti GPU and an AMD Ryzen 9 5900X CPU. In the cryo-EM model, missing residues in the holo cryo-EM structure, including the first 10 N-terminal residues and the cpmApple 26-residue loop region (Ser270-Met295), were grafted from the AlphaFold2 (AF2) model. For the holo MD simulations, the topology was prepared by protonating the protein chains at a physiological pH of 7.4 and/or by adding missing hydrogen using Desmond's Protein Preparation tool. Each system was then solvated in an orthorhombic TIP3P water box with a minimum 18 Å buffer from the protein surface and neutralized with K⁺/Cl⁻ ions at 150 mM. Energy minimization was performed for 200 ps at the beginning (0 ns) and for 150 ps at 50 ns, after which the systems were relaxed under default NPT settings (1 ps Nose-Hoover chain thermostat, 2 ps Martyna-Tobias-Klein barostat, 2 fs RESPA timesteps, and a 9 Å Coulombic cutoff without restraints). MD simulations were subsequently run for a total of 500 ns (50 ns equilibration followed by 450 ns Production MD simulations), with trajectory frames recorded every 100 ps. Holo trajectories were clustered into 10 groups using Desmond's clustering tool, and the final 400 ns of each simulation were analyzed using Desmond's Simulation Interaction Diagram (SID) tool to generate plots of root-mean-square deviation (RMSD), rootmean-square fluctuation (RMSF), and chromophore interactions with surrounding residues. The apo structure was obtained by removing Ca²⁺ and L-lactate from the most populated holo pose derived from the AF2 simulation and modifying the chromophore to its phenolic state. To prevent trapping in local minima, Replica Exchange Molecular Dynamics (REMD) was performed using Desmond's REMD tool with a parallel tempering approach. Sixteen replicas were distributed across a linear temperature range from 287.0 K to 371.0 K (increments of ~5.6 K) and run for 150 ns (100 ns + 50 ns), with trajectories recorded every 100 ps. The REMD system was solvated in an orthorhombic TIP3P water box with a minimum 18 Å buffer from the protein surface and underwent 200 ps of minimization before being relaxed under default NPT conditions. The final 50 ns of REMD trajectories were clustered into five groups, with the most populated cluster selected for subsequent apo MD simulations. These apo simulations followed the same parameters as the holo simulations, running for 550 ns (50 ns equilibration and 500 ns production) with trajectory frames recorded every 100 ps, and duplicate simulations were performed. The final 500 ns of each apo simulation were clustered into 10 groups using Desmond's clustering tool, and the final 400 ns of trajectories from both apo simulations were analyzed using the SID tool to generate RMSD, RMSF, and chromophore-residue interaction plots.

Construction of mammalian expression vectors

For cell surface expression, the genes encoding R-eLACCO2, R-eLACCO2.1, and R-deLACCO_{ctrl} were amplified by PCR followed by digestion with BglII and EcoRI, and then ligated into a pcDNA3.1 vector (Thermo Fisher Scientific) that contains N-terminal leader sequence and C-terminal anchor. To construct CD59-anchored R-eLACCO2.1 with various leader sequences, complementary oligonucleotides (Thermo Fisher Scientific) encoding each leader sequence were digested by XhoI and BglII, and then ligated into a similarly-digested pcDNA3.1, including CD59-anchored R-eLACCO2.1. The gene encoding PDGFR transmembrane domain was amplified by PCR using pDisplay vector (Thermo Fisher Scientific) as a template, and then substituted with the CD59 GPI domain of the pcDNA3.1 product above by using EcoRI and HindIII. To construct R-eLACCO plasmids for expression in neurons and astrocytes, the gene encoding R-eLACCO variants, including the Igk leader and COBRA GPI anchor sequence in the pcDNA3.1 vector was first amplified by PCR followed by digestion with NheI and XhoI, and then ligated into pAAV plasmid containing the hSyn and gfaABC1D promoter.

Imaging of R-eLACCO variants in HEK293T, HeLa and T98G cell lines

HEK293T (Thermo Fisher Scientific, #R70007) and HeLa (American Type Culture Collection, ATCC, #CCL-2) cells were maintained in Dulbecco's modified Eagle medium (DMEM; Nakalai Tesque) supplemented with 10% fetal bovine serum (FBS; Sigma-Aldrich) and 1% penicillin-streptomycin (Nakalai Tesque) at 37 °C and 5% CO₂. T98G cells (ATCC, #CRL-1690) were maintained in minimum essential medium (Nakalai Tesque) supplemented with 10% FBS, 1% penicillin-streptomycin, 1% non-essential amino acid (Nakalai Tesque), and 1 mM sodium pyruvate (Nakalai Tesque) at 37 °C and 5% CO₂. Cells were transiently transfected with the constructed plasmid using polyethyleneimine (PEI, Polysciences). Transfected cells were imaged using an IX83 wide-field fluorescence microscopy (Olympus) equipped with a pE-300 LED light source (CoolLED), a 40× objective lens (numerical aperture (NA) = 1.3; oil), an ImagEM X2 EM-CCD camera (Hamamatsu), Cellsens software (Olympus), and a STR stage incubator (Tokai Hit). The filter sets used in live cell imaging had the following specifications: iLACCO1 and EGFP: excitation 470/20 nm, dichroic mirror 490-nm dclp, and emission 518/45 nm; R-eLACCO variants and mApple: excitation 545/20 nm, dichroic mirror 565-nm dclp, and emission 598/55 nm. Fluorescence images were analyzed with Imagel software (National Institutes of Health).

For the optimization of leader and anchor, HEK293T cells were cotransfected with respective R-eLACCO2.1 genes and pAMEXT-EGFP. Measurement of individual fluorescence distribution profiles and calculation of the Pearson correlation coefficient were carried out as follows: a linear region of interest (ROI) was generated on the cell of interest to cross the membrane manually. The fluorescence distribution of ROI was measured from both the R-eLACCO stack and the GFP marker stack using the Plot Profile function (ImageJ2, ver. 2.3.0/1.53q). After measuring the raw values, the fluorescence profile data from both stacks were combined. The correlation functions were calculated as the Pearson Correlation score expressed by the *corr* function in Pandas (ver. 1.5.3).

For L-lactate bath application to measure in situ K_d and response kinetics, HeLa cells seeded onto coverslips were transfected with R-eLACCO variants. Forty-eight hours after transfection, the

transfected HeLa cells were washed twice with Hank's balanced salt solution (HBSS(+): Nakalai Tesque), and then the coverslips were transferred into Attofluor™ Cell Chamber (Thermo Fisher Scientific, Cat. #A7816) with HBSS(+) supplemented with 10 mM HEPES (Nakalai Tesque) and 1 µM AR-C155858 (Wako). Exchange of bath solutions during the imaging (interval time: 30 s. exposure time: 100-200 ms) was performed in a remove-and-add manner using a homemade solution remover⁶⁵ just after the first 4 images were acquired, and completed in approximately 20 s. This dead time can result in overestimation of the absolute values of τ_{on} and τ^{off} . The plots were fitted with a single exponential function. For the photostability test, R-eLACCO variants or mapple was expressed on the surface of HeLa cells and illuminated by excitation light at 100% intensity of LED (~4 mW cm⁻² at 560 nm on the objective lens) using one-photon widefield microscopy, and then their fluorescence images were recorded at 37 °C for 4 min with the exposure time of 50 ms and no interval time. For blue-light-mediated photoactivation, HeLa cells transfected with R-eLACCO variants were imaged under intermittent illumination (exposure time for 200 ms per illumination) of LED light filtered with 470/20 bandpath (~4 mW cm⁻² on the objective lens).

For imaging of Ca²⁺-dependent fluorescence, HeLa cells seeded onto coverslips were transfected with R-eLACCO variants. Forty-eight hours after transfection, the coverslips were transferred into AttofluorTM Cell Chamber with HBSS(-) buffer (Nakalai Tesque) supplemented with 10 mM HEPES and 10 mM L-lactate. Other bath solutions were supplemented with Ca²⁺ of 100 nM, 1 μ M, 10 μ M, 100 μ M, 300 μ M, 1 mM, 3 mM, and 10 mM. Rapid change of bath solutions during the image was performed in a remove-and-add manner using a homemade solution remover⁶⁵.

For imaging of caged L-lactate, HeLa cells seeded onto a glass-bottom dish were transfected with R-eLACCO variants. Forty-eight hours after transfection, the imaging was performed in HBSS(+) buffer supplemented with 10 mM HEPES, 1 μ M AR-C155858, and 1 mM MNI-L-lactate (1% DMSO). For photoactivation, polygon1000 DMD system (Migtex) equipped with 405-nm LED (UHP-F-405, Prizmatix, 2.4 mW cm $^{-2}$ on the objective lens) was used to illuminate for 1 s.

Fluorescence lifetime imaging microscopy (FLIM)

For in vitro experiments, the fluorescence lifetime was measured using an FV1200 confocal microscope (Olympus) equipped with rapidFLIMHIRes with a MultiHarp 150 Time-Correlated Single Photon Counting (TCSPC) unit (PicoQuant) and an air objective lens (UPLFLN 10×, NA = 0.3, Olympus). A 560 nm pulse laser (PicoQuant) was used for excitation and collected fluorescence emission through a bandpass filter (600/50 nm, Bright Line HC). The scanning resolution was set at 256 × 256 pixels with a scanning time of 0.429 seconds per frame. In a 96-well plate (3860-096, IWAKI), 100 µL purified proteins with the final concentration of 1 µM in 30 mM MOPS, 100 mM KCl, 1 mM CaCl₂, pH 7.2, with and without 100 mM L-lactate, were measured the fluorescence lifetime. For pH titration, the pH buffers containing 30 mM trisodium citrate, 30 mM sodium borate, 30 mM MOPS, 100 mM KCl, 1 mM CaCl₂, and either no L-lactate or 100 mM L-lactate, were used. For HeLa cell experiments, FLIM imaging was conducted with the same FLIM microscope above with an oil immersion objective lens (PLAPON $60\times$, NA = 1.42, Olympus), and the scanning resolution was set at $512\times$ 512 pixels with a scanning time of 1.109 s per frame. The cells were seeded on homemade glass-bottom dishes. Upon reaching 50-60% confluence, the cells were transfected with 1 µg plasmid and 2.5 µg of PEI in an opti-MEM medium. After 6 hours, the medium was replaced with fresh DMEM supplemented with 10% FBS and 1% penicillinstreptomycin. The cells were then cultured for 48 hours in a 37 °C incubator supplied with 5% CO₂. Prior to imaging, the cells were washed three times with PBS and replaced the medium with HBSS(+) supplemented with 10 mM HEPES, pH 7.4 (Nakalai Tesque) and 1 µM AR-C155858 (Wako). The cells were then treated with L-lactate to a final

concentration of 10 mM and captured 40 frames of fluorescence lifetime images after a 5-min treatment period. For the calculation of fluorescence lifetime values, analysis was conducted using the Sym-PhoTime 64 software (PicoQuant, version 2.8). The fluorescence lifetime decay histogram was fitted with a two-exponential function, with the arrival time fixed to 0–8 ns, starting from the pulse laser⁶⁶. Finally, the intensity-weighted average lifetime was reported.

Dual-color FLIM imaging of T98G cells expressing R-eLACCO2.1 and LiLac 22 was conducted using a Stellaris 8 FALCON confocal microscope (Leica) equipped with an oil immersion objective lens (PLAPO 63×, NA=1.40, Leica) and a white light laser. The excitation and emission wavelength used in the imaging had the following specifications: R-eLACCO2.1: excitation 561 nm and emission 565-703 nm; LiLac: excitation 448 nm and emission 455-550 nm.

Packaging and purification of adeno-associated viruses (AAVs)

AAVs were generated in HEK293T17 cells by triple transfection of a helper plasmid pXX680, a plasmid encoding either the AAV2/5 or AAV2/9 rep/cap, and a pAAV plasmid encoding the corresponding R-eLACCO biosensor. Forty-eight hours post-transfection, the cells were harvested by gentle scraping and pelleted by centrifugation. Viral particles were released by four freeze-thaw cycles on dry-ice/ethanol and free DNA was digested with benzonase. The AAV particles were purified by a discontinuous gradient of iodixanol (15-25-40-60%) and ultracentrifugation (462,000 × g for 70 min at 16 °C). The viral preparation was then washed and concentrated through a 100 kDa Amicon filter. During the last concentration step, the buffer was adjusted to 5% D-sorbitol and 0.001% pluronic acid for storage and experimentation. Titration was performed by TaqMan digital droplet-PCR using primers specific for AAV2 inverted terminal repeat (ITR).

Imaging of R-eLACCO variants in primary neurons and astrocytes

Male and female pups were obtained from a single timed-pregnant Sprague Dawley rat (Charles River Laboratories, purchased from Japan SLC, Inc.). Experiments were performed with cortical/hippocampal primary cultures from the E21 (after C-section of the pregnant rat) plated in glass-bottom 24-well plates (Cellvis) where 0.5×10^6 cells were used for three wells. Cultures were nucleofected at the time of plating with Nucleofector 4D (Lonza), and imaged 14 days later. Three wells were plated and imaged per nucleofected construct. Neurons were cultured in NbActive4 medium (BrainBits) supplemented with 1% penicillin-streptomycin at 37 °C and 5% CO₂. Astrocytes were cultured in DMEM supplemented with 10% FBS and 1% penicillin-streptomycin at 37 °C and 5% CO₂. Culture media were replaced with 1 mL of imaging buffer (145 mM NaCl, 2.5 mM KCl, 10 mM glucose, 10 mM HEPES, 2 mM CaCl₂, 1 mM MgCl₂, pH 7.4) for imaging²⁴.

For another imaging of neurons, primary embryonic rat cortical neurons were isolated from euthanized pregnant Sprague-Dawley rats (Charles River) at embryonic day 18 (Ref. 67). Embryos were harvested by Cesarean section and cerebral cortices were isolated and dissociated with 0.25% trypsin without EDTA (Invitrogen, #15090-046) by digestion for 15 min at 37 °C and trituration with 1 mL plastic tip. Poly-D-lysine (Sigma, #P-1149)-coated 96-well glass bottom plates (Cellvis, #P96-1.5H-N) were seeded with 15,000 cells per well in Neurobasal medium (Invitrogen, #21103-049) supplemented with 10% heatinactivated FBS (Gibco), 0.5 mM GlutaMAXTM (Gibco, #35050079), 100 IU mL⁻¹ penicillin, and 100 μg mL⁻¹ streptomycin (Gibco). Before seeding, cells were counted using the Automated cell counter TC10 (Bio-Rad), and viability (90–95%) was checked with Trypan Blue Stain (0.4%, Gibco #15250-061). After 1 h incubation in a CO₂ incubator at 37 °C, the media was changed to Neurobasal medium supplemented with B27 (Invitrogen, #17504044) and 0.5 mM GlutaMAX[™]. One-half of the media was changed twice each week. Lipid-mediated transient transfection of the neurons with R-eLACCO constructs was performed

on DIV (days in vitro) 12 using Lipofectamine 2000 (Thermo Fisher Scientific, #11668027)⁶⁸. Twenty-four hours post-transfection, the culture media were replaced with imaging buffer (145 mM NaCl, 2.5 mM KCl, 10 mM D-glucose, 10 mM HEPES, 2 mM CaCl₂, 1 mM MgCl₂, pH 7.4). Automated high-throughput live cell microscopy was carried out with the ImageXpress (Molecular Devices) using a TRITC filter set and S Fluor 20×/0.45 NA air objective (Nikon). We recorded changes in R-eLACCO fluorescence and determined mean fluorescence intensities by tracing the outer soma perimeter of individual neurons using Fiji software before and after 10 mM L-lactate addition.

Suprachiasmatic nucleus (SCN) slice imaging⁶⁹

Wild-type C57BL/6 J mice were purchased from Charles River. Pups were maintained at 20-24 °C with 45-65% humidity in a 12:12 lightdark cycle together with their mothers before being sacrificed at P11-15 via cervical dislocation. Food and water were provided ad libitum. Organotypic SCN cultures were prepared and transduced as described in Ref. 70. Briefly, the brain was isolated and dissected in GBSS (Sigma, #G9779) supplemented with 5 mg mL⁻¹ D-glucose (Sigma, #158968), 100 nM MK801 (Sigma, #M107), 3 mM MgCl₂ (Invitrogen, #AM9530G), and 50 µM AP-5 (Tocris, #0106). The SCN was extracted from coronal sections of 300 µm thickness and placed on a tissue culture insert (Merck, #PICMORG50). Slices were kept in DMEMbased medium (1x, Sigma #D5030) supplemented with 100 nM MK801, 3 mM MgCl₂, and 50 µM AP-5 for 2-3 h, and then cultured in DMEM-based medium with 4.17 mM NaHCO₃, 15 mM D-glucose, 1× penicillin/streptomycin (Sigma, #P4333), 10 mM HEPES (Sigma, #H0887), 5% FBS (Gibco, #10270106), 1% B27 (Gibco, #17504044), and 0.5% Glutamax (Invitrogen, #35050-038) while kept sealed at 37 °C. Slices were transduced one week after isolation via direct addition of 1.5 µL of AAV2/9-hSyn-R-eLACCO2.1 or AAV2/9-hSyn-R-deLACCO_{ctrl} onto the tissue. Fluorescence imaging was performed in a Sartorius Incucyte S3 imaging system one-week post-transduction. SCN slices were imaged in a 6-well plate. Images were acquired at 4× magnification with fluorescence acquired over 300 ms every 15 or 30 mins. For L-lactate treatment, the SCN slices were briefly removed from the incubation chamber of the imaging system and were returned in to the system that contains the medium containing 10 mM or 40 mM L-lactate (Sigma, #71718). Note that the temperature for the SCN slices slightly changes during this procedure. Image series were registered and background subtracted using ImageJ. Time series were extracted from a region of interest covering the SCN.

In vivo imaging

Awake imaging was done in male and female wild-type mice (bred from C57BL/6 J from Jackson Laboratory at 20–26 °C with 30–70% humidity in a 12:12 light-dark cycle, food and water provided ad libitum) at an age of 4-9 months. Mice were anesthetized with isoflurane using a precision vaporizer, 4% (vol/vol) in oxygen for induction, and 1-2% (vol/vol) for maintenance and given the analgesic buprenorphine subcutaneously (0.1 μg g⁻¹ body weight). The animal was mounted on a stereotaxic frame, and the body temperature was maintained at 36-37 °C with a heating pad during anesthesia. A 3.5-mm craniotomy was created over the right vS1 cortex (centroid at 1.5 mm posterior to the bregma and 3.4 mm lateral from the midline) while avoiding damage to the dura. Glass pipettes (Drummond, #QF100-60-10) were pulled (Sutter Instruments, #P-2000) and beveled to a tip at 10–20 μm outer diameter with fine scissors. At multiple locations within vS1 cortex, 50–150 nL AAV (AAV2/9-hSyn-R-eLACCO2.1 titer 1.8×10^{12} GC mL⁻¹) was injected 400–500 μm below the dura using a motorized manipulator (Sutter Instruments, #MPC-200, #MP285/M-21826, and #ROE-200) using a syringe pump (KD Scientific, #Legato 185). For simultaneous L-lactate and Ca²⁺ imaging, AAV2/9-hSyn-R-eLACCO2.1 was mixed with hSyn-cre AAV (Addgene, #105553-AAV8, hSyn-cre-WPRE-hGH) and injected into two heterozygous mice conditionally

expressing GCaMP6f (Jackson Laboratory, #028865). A cranial window was custom-made with a 3.5 mm round coverslip (no. 1 CS-3.5 R. Warner Instruments, #64-0739) and was glued to a 5 mm round coverslip (no. 1 CS-5R, Warner Instruments, #64-0700) using Norland Optical Adhesive NOA 61, embedded in the craniotomy, and sealed with cyanoacrylate glue (Loctite, #401), Metabond (Parkell L-Powder and Ouick Base) was further applied around the edge to reinforce stability. A custom-designed titanium head-bar was attached to the skull with Metabond, and the remaining exposed bone was covered with dental acrylic (Lang Ortho-Jet). In vivo imaging was carried out after 1-6 months of expression and at least three 1-hour sessions of habituation for head fixation. All imaging experiments used head-fixed awake mice under adaptive optics two-photon microscopy (AO2P) with correction using a deformable mirror for aberration originating in the microscope⁷¹. The femtosecond pulsed laser Chameleon Discovery NX (Coherent) was tuned to 930 nm (eLACCO2.1), 1,030 nm (simultaneous imaging of GCaMP6f and R-eLACCO2.1), or 1,100 nm (ReLACCO2.1) for excitation. To minimize potential interference from functional hyperemia for simultaneous L-lactate and Ca²⁺ imaging, the cells in yellow circles (Fig. 6f) were selectively analyzed by postimaging with Cy5.5 blood plasma labeling. A 25× objective (Olympus, XLPlanN), dichroic mirrors (FF775-Di01 and FF662-Di01), filters (FF01-593/46 and FF01-240-sp), and MPPC modules (Hamamatsu 20A-002) were used for emission detection at 1 Hz on a resonant-galvo scanner. The use of the FF01-593/46 filter aimed to reduce bleedthrough from the GCaMP6f signal, though it was not completely eliminated. The relatively dimmer fluorescence of R-deLACCO_{ctrl} results in more pronounced bleedthrough effects than R-eLACCO2.1. Post-objective power was kept under 40 mW for all measurements. The dura was aligned to the imaging plane using two goniometers (GNL10/M) under an episcope (Zeiss Stereo, X-Cite 120Q). Tail vein catheters (custommade 30 G needle connected to PE10 tubing) were placed under isoflurane 1.5% and after 5 minutes of tail warming at 37 °C, successful intravenous placement was tested using 50 µL saline injection before letting the mouse wake up. Calibrated syringe pumps were connected using PE10 tubing and Y-connectors (Instechlab, #SCY-25) for saline and L-lactate (Sigma, #L7022) infusions.

One photon frame-based imaging utilized a SteREO Discovery V8 (Zeiss) equipped with a custom filter cube (KSC 295-CUSTOM, Kramer Scientific, LLC) carrying a reflective mirror and ZET488/561 m emission filter (Chroma). A LED was coupled to a liquid lightguide (565 nm center wavelength, ThorLabs, SOLIS-4C; Semrock, FF01-560/14-25). Image acquisition was performed with a Prime95B 1200 × 1200 sCMOS camera (Teledyne Photometrics) with the software MicroManager 2. For somatosensory stimulation, air puffs were directed to all vibrissae contra-lateral to the imaging window with valve opening (5 PSI, Parker Hannifin 004-0008-900) for 10 ms puffs separated by 150 ms delays for 20 seconds. The location of the barrel cortex was confirmed using intrinsic optical imaging⁷². A pupil was recorded (Basler, #106752-16) with IR LED illumination and blue LED background light adjusted to pre-constrict the pupil. Four points on the circumference were mapped using DeepLabCut (ver. 2), and a circle was fitted to extract the pupil diameter. Locomotion speed was measured using an incremental encoder (TRD-MX1024BD). Image acquisition, locomotion, pupil diameter, and vibrissa stimulation were tracked using LabChart (ADInstruments, ver. 8) and analyzed using Matlab (MathWorks, 2019-2025). Translational transformation was used to register each frame to a smoothed, averaged frame at the start of each trial for motion correction, and frames with excess translation vector (>1 s.d.) were excluded and interpolated. Locomotion and Ca²⁺ events larger than 2 s.d. were considered significant.

For in vivo calibration, a guide cannula was implanted in the surface of the vS1 cortex in three mice. After a week, an electrochemical probe specific for L-lactate (Pinnacle Technology, #7004-80) was precalibrated ex vivo using L-lactate and ascorbic acid at 37 °C and was

inserted into the cortex under isoflurane 2%. After four hours of recovery, a tail vein catheter was placed under isoflurane 2% for awake imaging. Saline and L-lactate dissolved in saline at 1 M were injected in mice using the following volumes: $100 \,\mu\text{L}$ (saline), $6.25 \,\mu\text{L}$ (0.25 mmol kg⁻¹), $12.5 \,\mu\text{L}$ (0.5 mmol kg⁻¹), $25 \,\mu\text{L}$ (1.0 mmol kg⁻¹), $50 \,\mu\text{L}$ (2.0 mmol kg⁻¹), and $100 \,\mu\text{L}$ (4.0 mmol kg⁻¹).

Statistics and reproducibility

All data are expressed as mean \pm s.d. or mean \pm s.e.m., as specified in figure legends. Box plots are used for Figs. 2b,d, 3c,f-h,p, 4c,f, 5f, and 6c. In these box plots, the horizontal line is the median; the top and bottom horizontal lines are the 25th and 75th percentiles for the data; and the whiskers extend one standard deviation range from the mean represented as black filled circle. Sample sizes (n) are listed with each experiment. No samples were excluded from analysis and all experiments were reproducible. For pharmacological specificity, statistical analysis was performed using one-way analysis of variance (ANOVA) with Dunnett's post hoc tests (Igor Pro 8). In photobleaching experiments, group differences were analyzed using one-way ANOVA followed by Tukey's multiple comparison (GraphPad Prism 9). Statistical analyses for in situ kinetics analysis and the slice imaging were conducted with two-tailed unpaired Student t-test and Welch's unpaired ttest, respectively (GraphPad Prism 9). Microsoft Excel software was used to plot for Figs. 1c,d,f,h,k,l, and 3p.

Ethical statement

For experiments performed at The University of Tokyo, all methods for animal care and use were approved by the institutional review committees of the School of Science, The University of Tokyo. Experiments on organotypic SCN slices were carried out in accordance with regulations of the UK Home Office under the Animals (Scientific Procedures) Act 1986, with Local Ethical Review by the Imperial College London Animal Welfare and Ethical Review Body Standing Committee (AWERB). For experiments performed at Northwestern University, the protocol was approved by the Northwestern University administrative panel on laboratory animal care. All experiments performed at the University of California, San Diego have been approved by the Institutional Animal Care and Use Committee at the University of California, San Diego.

Data availability

The plasmids generated in this study have been deposited in Addgene (https://www.addgene.org/browse/article/28248379/). Structure coordinates of R-eLACCO2 have been deposited in the Protein Data Bank with a code of 8ZMZ. The cryo-EM density map of R-eLACCO2 has been deposited in the Electron Microscopy Data Bank under the accession code EMD-60263. Previously published protein structures used in this work include PDB 7E9Y and 4I2Y. Source data are provided with this paper.

References

- Fitts, R. H. & Holloszy, J. O. Lactate and contractile force in frog muscle during development of fatigue and recovery. *Am. J. Physiol.* 231, 430–433 (1976).
- Fletcher, W. M. Lactic acid in amphibian muscle. J. Physiol. 35, 247–309 (1907).
- Ferguson, B. S. et al. Lactate metabolism: historical context, prior misinterpretations, and current understanding. Eur. J. Appl. Physiol. 118, 691–728 (2018).
- Murphy, R. M., Watt, M. J. & Febbraio, M. A. Metabolic communication during exercise. *Nat. Metab.* 2, 805–816 (2020).
- Bonvento, G. & Bolaños, J. P. Astrocyte-neuron metabolic cooperation shapes brain activity. Cell Metab. 33, 1546–1564 (2021).
- Mächler, P. et al. In Vivo Evidence for a Lactate Gradient from Astrocytes to Neurons. Cell Metab. 23, 94–102 (2016).

- Magistretti, P. J. & Allaman, I. Lactate in the brain: from metabolic end-product to signalling molecule. *Nat. Rev. Neurosci.* 19, 235–249 (2018).
- Jimenez-Blasco, D. et al. Glucose metabolism links astroglial mitochondria to cannabinoid effects. Nature 583, 603–608 (2020).
- 9. Demetrius, L. A., Magistretti, P. J. & Pellerin, L. Alzheimer's disease: the amyloid hypothesis and the Inverse Warburg effect. *Front. Physiol.* **5**, 522 (2014).
- Powell, C. L., Davidson, A. R. & Brown, A. M. Universal Glia to Neurone Lactate Transfer in the Nervous System: Physiological Functions and Pathological Consequences. *Biosensors* 10, (2020).
- Díaz-García, C. M. et al. Neuronal stimulation triggers neuronal glycolysis and not lactate uptake. Cell Metab. 26, 361–374.e4 (2017).
- Zuend, M. et al. Arousal-induced cortical activity triggers lactate release from astrocytes. Nat. Metab. 2, 179–191 (2020).
- Nasu, Y., Shen, Y., Kramer, L. & Campbell, R. E. Structure- and mechanism-guided design of single fluorescent protein-based biosensors. *Nat. Chem. Biol.* 17, 509–518 (2021).
- San Martín, A. et al. A genetically encoded FRET lactate sensor and its use to detect the Warburg effect in single cancer cells. *PLoS One* 8, e57712 (2013).
- Aburto, C. et al. Single-Fluorophore Indicator to Explore Cellular and Sub-cellular Lactate Dynamics. ACS Sens https://doi.org/10. 1021/acssensors.2c00731 (2022).
- Li, X. et al. Ultrasensitive sensors reveal the spatiotemporal landscape of lactate metabolism in physiology and disease. *Cell Metab*. https://doi.org/10.1016/j.cmet.2022.10.002 (2022).
- 17. Bekdash, R. et al. GEM-IL: A highly responsive fluorescent lactate indicator. *Cell Rep. Methods* **1**, 100092 (2021).
- Harada, K. et al. Green fluorescent protein-based lactate and pyruvate indicators suitable for biochemical assays and live cell imaging. Sci. Rep. 10, 19562 (2020).
- 19. Xu, X. et al. A selective fluorescent l-Lactate biosensor based on an l-Lactate-specific transcription regulator and förster resonance energy transfer. *Biosensors* 12, 1111 (2022).
- Nasu, Y. et al. Lactate biosensors for spectrally and spatially multiplexed fluorescence imaging. Nat. Commun. 14, 6598 (2023).
- Chang, X. et al. A bright red fluorescent genetically encoded sensor for lactate imaging. *Biochem. Biophys. Res. Commun.* 734, 150449 (2024).
- Koveal, D. et al. A high-throughput multiparameter screen for accelerated development and optimization of soluble genetically encoded fluorescent biosensors. *Nat. Commun.* 13, 2919 (2022).
- Nasu, Y. et al. A genetically encoded fluorescent biosensor for extracellular L-lactate. Nat. Commun. 12, 7058 (2021).
- Chen, T.-W. et al. Ultrasensitive fluorescent proteins for imaging neuronal activity. Nature 499, 295–300 (2013).
- Akerboom, J. et al. Genetically encoded calcium indicators for multi-color neural activity imaging and combination with optogenetics. Front. Mol. Neurosci. 6, 2 (2013).
- Silver, I. A. & Erecińska, M. Intracellular and extracellular changes of [Ca2+] in hypoxia and ischemia in rat brain in vivo. *J. Gen. Physiol.* 95, 837–866 (1990).
- Dean, K. M. et al. Analysis of red-fluorescent proteins provides insight into dark-state conversion and photodegradation. *Biophys. J.* 101, 961–969 (2011).
- 28. Hario, S. et al. High-Performance Genetically Encoded Green Fluorescent Biosensors for Intracellular l-Lactate. ACS Cent. Sci. https://doi.org/10.1021/acscentsci.3c01250 (2024).
- Miyazaki, I. et al. Synthesis and application of a photocaged-Llactate for studying the biological roles of L-lactate. Commun. Chem. 8, 104 (2025).
- 30. Vu, C. Q. & Arai, S. Quantitative imaging of genetically encoded fluorescence lifetime biosensors. *Biosensors* **13**, (2023).

- Cohen, J. E. & Fields, R. D. Extracellular calcium depletion in synaptic transmission. *Neuroscientist* 10, 12–17 (2004).
- Zhao, Y. et al. An expanded palette of genetically encoded Ca²⁺ indicators. Science 333, 1888–1891 (2011).
- Aggarwal, A. et al. Glutamate indicators with improved activation kinetics and localization for imaging synaptic transmission. *Nat. Methods* https://doi.org/10.1038/s41592-023-01863-6 (2023).
- Unger, E. K. et al. Directed evolution of a selective and sensitive serotonin sensor via machine learning. Cell 183, 1986–2002.e26 (2020).
- Sun, F. et al. A Genetically Encoded Fluorescent Sensor Enables Rapid and Specific Detection of Dopamine in Flies, Fish, and Mice. Cell 174, 481–496.e19 (2018).
- Wang, H. et al. A tool kit of highly selective and sensitive genetically encoded neuropeptide sensors. Science 382, eabq8173 (2023).
- Patriarchi, T. et al. Ultrafast neuronal imaging of dopamine dynamics with designed genetically encoded sensors. Science 360, (2018).
- Kagiampaki, Z. et al. Sensitive multicolor indicators for monitoring norepinephrine in vivo. Nat. Methods 20, 1426–1436 (2023).
- Magistretti, P. J. & Schorderet, M. Norepinephrine and histamine potentiate the increases in cyclic adenosine 3':5'-monophosphate elicited by vasoactive intestinal polypeptide in mouse cerebral cortical slices: mediation by alpha 1-adrenergic and H1histaminergic receptors. J. Neurosci. 5, 362–368 (1985).
- Dienel, G. A. & Cruz, N. F. Aerobic glycolysis during brain activation: adrenergic regulation and influence of norepinephrine on astrocytic metabolism. *J. Neurochem.* 138, 14–52 (2016).
- Mosienko, V., Teschemacher, A. G. & Kasparov, S. Is L-lactate a novel signaling molecule in the brain?. J. Cereb. Blood Flow. Metab. 35, 1069–1075 (2015).
- Vaccari-Cardoso, B., Antipina, M., Teschemacher, A. G. & Kasparov, S. Lactate-Mediated Signaling in the Brain-An Update. *Brain Sci* 13, (2022).
- 43. Cerdán, S. et al. The redox switch/redox coupling hypothesis. *Neurochem. Int.* **48**, 523–530 (2006).
- Prichard, J. et al. Lactate rise detected by 1H NMR in human visual cortex during physiologic stimulation. *Proc. Natl. Acad. Sci. USA*. 88, 5829–5831 (1991).
- 45. Sappey-Marinier, D. et al. Effect of photic stimulation on human visual cortex lactate and phosphates using ¹H and ³¹P magnetic resonance spectroscopy. *J. Cereb. Blood Flow. Metab.* **12**, 584–592 (1992).
- Roumes, H. et al. Lactate transporters in the rat barrel cortex sustain whisker-dependent BOLD fMRI signal and behavioral performance. *Proc. Natl. Acad. Sci. USA.* 118, e2112466118 (2021).
- Hu, Y. & Wilson, G. S. A temporary local energy pool coupled to neuronal activity: fluctuations of extracellular lactate levels in rat brain monitored with rapid-response enzyme-based sensor. J. Neurochem. 69, 1484–1490 (1997).
- Wolfe, A. D. et al. Local and dynamic regulation of neuronal glycolysis in vivo. Proc. Natl. Acad. Sci. Usa. 121, e2314699121 (2024).
- Liu, H. & Naismith, J. H. An efficient one-step site-directed deletion, insertion, single and multiple-site plasmid mutagenesis protocol. BMC Biotechnol. 8, 91 (2008).
- Drobizhev, M., Molina, R. S. & Hughes, T. E. Characterizing the Twophoton Absorption Properties of Fluorescent Molecules in the 680-1300 nm Spectral Range. *Bio Protoc* 10, (2020).
- Dalangin, R. et al. Far-red fluorescent genetically encoded calcium ion indicators. bioRxiv 2020.11.12.380089. https://doi.org/10.1101/ 2020.11.12.380089 (2020).
- Molina, R. S. et al. Understanding the fluorescence change in red genetically encoded calcium ion indicators. *Biophys. J.* 116, 1873–1886 (2019).

- Barnett, L. M., Hughes, T. E. & Drobizhev, M. Deciphering the molecular mechanism responsible for GCaMP6m's Ca2+-dependent change in fluorescence. PLoS One 12. e0170934 (2017).
- Punjani, A., Rubinstein, J. L., Fleet, D. J. & Brubaker, M. A. cryoS-PARC: algorithms for rapid unsupervised cryo-EM structure determination. *Nat. Methods* 14, 290–296 (2017).
- 55. Punjani, A., Zhang, H. & Fleet, D. J. Non-uniform refinement: adaptive regularization improves single-particle cryo-EM reconstruction. *Nat. Methods* **17**, 1214–1221 (2020).
- Rosenthal, P. B. & Henderson, R. Optimal determination of particle orientation, absolute hand, and contrast loss in single-particle electron cryomicroscopy. *J. Mol. Biol.* 333, 721–745 (2003).
- Emsley, P. & Cowtan, K. Coot: model-building tools for molecular graphics. Acta Crystallogr. D. Biol. Crystallogr. 60, 2126–2132 (2004).
- Yamashita, K., Palmer, C. M., Burnley, T. & Murshudov, G. N. Cryo-EM single-particle structure refinement and map calculation using Servalcat. Acta Crystallogr D. Struct. Biol. 77, 1282–1291 (2021).
- Nicholls, R. A., Fischer, M., McNicholas, S. & Murshudov, G. N. Conformation-independent structural comparison of macro-molecules with ProSMART. *Acta Crystallogr. D. Biol. Crystallogr.* 70, 2487–2499 (2014).
- 60. Chen, V. B. et al. MolProbity: all-atom structure validation for macromolecular crystallography. *Acta Crystallogr. D. Biol. Crystallogr.* **66**, 12–21 (2010).
- Pettersen, E. F. et al. UCSF ChimeraX: Structure visualization for researchers, educators, and developers. *Protein Sci.* 30, 70–82 (2021).
- Shaw, D. E. A fast, scalable method for the parallel evaluation of distance-limited pairwise particle interactions. *J. Comput. Chem.* 26, 1318–1328 (2005).
- 63. Jorgensen, W. L., Maxwell, D. S. & Tirado-Rives, J. Development and testing of the OPLS all-atom force field on conformational energetics and properties of organic liquids. *J. Am. Chem. Soc.* **118**, 11225–11236 (1996).
- 64. Kaminski, G. A., Friesner, R. A., Tirado-Rives, J. & Jorgensen, W. L. Evaluation and reparametrization of the OPLS-AA force field for proteins via comparison with accurate quantum chemical calculations on peptides. J. Phys. Chem. B 105, 6474–6487 (2001).
- Zhang, S., He, L., Zhou, Y. & Wang, Y. Fluorescence-Based Ratiometric Measurement of CRAC Channel Activity in STIM-Orai-Overexpressing HEK-293 Cells. *Methods Mol. Biol.* 1843, 17–39 (2018).
- Arai, S. et al. qMaLioffG: A single green fluorescent protein FLIM indicator enabling quantitative imaging of endogenous ATP. bioRxiv 2023.08.29.555275 https://doi.org/10.1101/2023.08.29.555275 (2023).
- Shum, A. et al. Octopamine metabolically reprograms astrocytes to confer neuroprotection against α-synuclein. *Proc. Natl. Acad. Sci. USA.* 120, e2217396120 (2023).
- Chiu, A. M., Barse, L., Hubalkova, P. & Sanz-Clemente, A. An Antibody Feeding Approach to Study Glutamate Receptor Trafficking in Dissociated Primary Hippocampal Cultures. J. Vis. Exp. https://doi. org/10.3791/59982. (2019)
- 69. Ness, N., Díaz-Clavero, S., Hoekstra, M. M. B. & Brancaccio, M. Rhythmic astrocytic GABA production synchronizes neuronal circadian timekeeping in the suprachiasmatic nucleus. *EMBO J.* **44**, 356–381 (2025).
- Brancaccio, M., Maywood, E. S., Chesham, J. E., Loudon, A. S. I. & Hastings, M. H. A Gq-Ca2+ axis controls circuit-level encoding of circadian time in the suprachiasmatic nucleus. *Neuron* 78, 714–728 (2013).
- Liu, R., Li, Z., Marvin, J. S. & Kleinfeld, D. Direct wavefront sensing enables functional imaging of infragranular axons and spines. *Nat. Methods* 16, 615–618 (2019).



- Knutsen, P. M., Mateo, C. & Kleinfeld, D. Precision mapping of the vibrissa representation within murine primary somatosensory cortex. *Philos. Trans. R. Soc. Lond. B Biol. Sci.* 371, (2016).
- Cranfill, P. J. et al. Quantitative assessment of fluorescent proteins. Nat. Methods 13, 557–562 (2016).

Acknowledgements

The authors thank H. Kato, T. Igarashi, R. Kojima, S. Keller, M. Yamane, Z. Wenchao, A. Aggarwal, and T. Terai for technical support. Work at Academia Sinica (AS) was supported by AS intramural funds and the Japan Science and Technology Agency (PRESTO JPMJPR22E9 and CREST JPMJCR24T6 to Y.N., PRESTO JPMJPR22E4 to T.K. and CREST JPMJCR20E2 to O.N.). Work at the University of Tokyo was supported by the Japan Society for the Promotion of Science (19K15691 and 21K14738 to Y.N., 24K01621 to Y.N. and T.K., 22K15072 and 24K01961 to T.K., 19H01015 and 19H05633 to R.E.C.), The Precise Measurement Technology Promotion Foundation, and the Japan Agency for Medical Research and Development (Strategic Research Program for Brain Sciences JP21dm0207073 to T.T., Research Support Project for Life Science and Drug Discovery (Basis for Supporting Innovative Drug Discovery and Life Science Research (BINDS)) JP24ama121002 (support number 3272) and JP24ama121012). Work at Montana State University was supported by National Institutes of Health (NIH) grants UO1 NSO94246, U24 NS109107, and F31 NS108593. M.B. and N.N. are funded by the UK Dementia Research Institute (UKDRI-5007 to M.B.) through UK DRI Ltd, principally funded by the UK Medical Research Council, Imperial College London, and President's PhD Scholarship awarded to N.N. Work at Kanazawa University was supported by the Nakatani Foundation and the World Premier International Research Center Initiative (WPI).

Author contributions

Y.N. developed all R-eLACCO variants and performed characterization in vitro and in mammalian cells. Y.N. and Y.K. performed screening of leader and anchor sequences, and cell imaging. J.M. performed a molecular dynamics simulation. R.H. purified R-eLACCO1.1 protein for two-photon characterization. M.D. measured two-photon excitation spectra, extinction coefficient, and quantum yield. T.K. and A.F. measured transient absorption. I.M. performed imaging with MNI-L-lactate. H.S., Y.H., and T.T. supervised imaging of rat primary cells. E.G. and G.C. performed additional primary neuron imaging. M.Boisvert and M.-E.P. produced AAVs. N.N. and M.Brancaccio performed ex vivo imaging. C.Q.V. and S.A. performed FLIM characterization and imaging. Y.N. performed dual-color FLIM imaging. Y.K., T.K., and O.N. conducted cryo-

electron microscopy. P.M., Z.K., R.L., and D.K. imaged R-eLACCO2.1 in vivo. Y.N. supervised research. Y.N., R.E.C., P.M., and D.K. wrote the manuscript.

Competing interests

The authors declare no competing interests.

Additional information

Supplementary information The online version contains supplementary material available at https://doi.org/10.1038/s41467-025-64484-x.

Correspondence and requests for materials should be addressed to Yusuke Nasu.

Peer review information *Nature Communications* thanks the anonymous reviewers for their contribution to the peer review of this work. A peer review file is available.

Reprints and permissions information is available at http://www.nature.com/reprints

Publisher's note Springer Nature remains neutral with regard to jurisdictional claims in published maps and institutional affiliations.

Open Access This article is licensed under a Creative Commons Attribution-NonCommercial-NoDerivatives 4.0 International License, which permits any non-commercial use, sharing, distribution and reproduction in any medium or format, as long as you give appropriate credit to the original author(s) and the source, provide a link to the Creative Commons licence, and indicate if you modified the licensed material. You do not have permission under this licence to share adapted material derived from this article or parts of it. The images or other third party material in this article are included in the article's Creative Commons licence, unless indicated otherwise in a credit line to the material. If material is not included in the article's Creative Commons licence and your intended use is not permitted by statutory regulation or exceeds the permitted use, you will need to obtain permission directly from the copyright holder. To view a copy of this licence, visit https://creativecommons.org/licenses/by-nc-nd/4.0/.

© The Author(s) 2025

¹Department of Chemistry, School of Science, The University of Tokyo, Bunkyo-ku, Tokyo, Japan. ²Department of Physics, University of California San Diego, La Jolla, CA, USA. ³Department of Brain Science, Imperial College London, London, UK. ⁴UK Dementia Research Institute at Imperial College London, London, UK. ⁵WPI Nano Life Science Institute, Kanazawa University, Kanazawa, Japan. ⁶Department of Biological Sciences, School of Science, The University of Tokyo, Bunkyo-ku, Tokyo, Japan. ⁷Institute of Biological Chemistry, Academia Sinica, Nankang, Taipei, Taiwan. ⁸CERVO Brain Research Center, Laval University, Québec, QC, Canada. ⁹Department of Neurology, Northwestern University Feinberg School of Medicine, Chicago, IL, USA. ¹⁰Laboratory of Neuropathology and Neuroscience, Graduate School of Pharmaceutical Sciences, The University of Tokyo, Tokyo, Japan. ¹¹Institute of Post-LED Photonics, Tokushima University, Tokushima, Japan. ¹²Department of Anesthesiology and Intensive Care, Laval University, Québec, QC, Canada. ¹³Department of Microbiology and Cell Biology, Montana State University, Bozeman, MT, USA. ¹⁴Department of Neurobiology, University of California San Diego, La Jolla, CA, USA. ¹⁵Institute of Biochemical Sciences, National Taiwan University, Taipei, Taiwan. ¹⁶These authors contributed equally: Philipp Mächler, Natalie Ness, Cong Quang Vu, Tsukasa Kusakizako. □ e-mail: nasu@as.edu.tw